

VLTI-AMBER velocity-resolved aperture-synthesis imaging of η Carinae with a spectral resolution of 12 000.

Studies of the primary star wind and innermost wind-wind collision zone^{★ ★★}

G. Weigelt¹, K.-H. Hofmann¹, D. Schertl¹, N. Clementel², M.F. Corcoran^{3,4}, A. Damineli⁵, W.-J. de Wit⁶, R. Grellmann⁷, J. Groh⁸, S. Guieu⁶, T. Gull⁹, M. Heininger¹, D.J. Hillier¹⁰, C.A. Hummel¹¹, S. Kraus¹², T. Madura⁹, A. Mehner⁶, A. Mérand⁶, F. Millour¹³, A.F.J. Moffat¹⁴, K. Ohnaka¹⁵, F. Patru¹⁶, R.G. Petrov¹³, S. Rengaswamy¹⁷, N.D. Richardson¹⁸, T. Rivinius⁶, M. Schöller¹¹, M. Teodoro⁹, and M. Wittkowski¹¹

(Affiliations can be found after the references)

Received September 15, 1996; accepted March 16, 1997

ABSTRACT

Context. The mass loss from massive stars is not understood well. η Carinae is a unique object for studying the massive stellar wind during the Luminous Blue Variable phase. It is also an eccentric binary with a period of 5.54 yr. The nature of both stars is uncertain, although we know from X-ray studies that there is a wind-wind collision whose properties change with orbital phase.

Aims. We want to investigate the structure and kinematics of η Car's primary star wind and wind-wind collision zone with a high spatial resolution of ~ 6 mas (~ 14 au) and high spectral resolution of $R = 12\,000$.

Methods. Observations of η Car were carried out with the ESO Very Large Telescope Interferometer (VLTI) and the AMBER instrument between approximately five and seven months before the August 2014 periastron passage. Velocity-resolved aperture-synthesis images were reconstructed from the spectrally dispersed interferograms. Interferometric studies can provide information on the binary orbit, the primary wind, and the wind collision.

Results. We present velocity-resolved aperture-synthesis images reconstructed in more than 100 different spectral channels distributed across the Bry 2.166 μm emission line. The intensity distribution of the images strongly depends on wavelength. At wavelengths corresponding to radial velocities of approximately -140 to -376 km s^{-1} measured relative to line center, the intensity distribution has a fan-shaped structure. At the velocity of -277 km s^{-1} , the position angle of the symmetry axis of the fan is $\sim 126^\circ$. The fan-shaped structure extends approximately 8.0 mas (~ 18.8 au) to the southeast and 5.8 mas (~ 13.6 au) to the northwest, measured along the symmetry axis at the 16% intensity contour. The shape of the intensity distributions suggests that the obtained images are the first direct images of the innermost wind-wind collision zone. Therefore, the observations provide velocity-dependent image structures that can be used to test three-dimensional hydrodynamical, radiative transfer models of the massive interacting winds of η Car.

Key words. Stars: winds, outflows – stars: individual: η Carinae – stars: massive – stars: mass-loss – binaries: general – techniques: interferometric

1. Introduction

Studies of the mass-loss process are of crucial importance for improving our understanding of stellar evolution. Infrared long-baseline interferometry provides us with a unique opportunity to study the mass loss from the colliding wind binary η Car. The primary star of the system is an extremely luminous and massive ($M \sim 100 M_\odot$) unstable Luminous Blue Variable star (LBV) with a high mass-loss rate of $\sim 10^{-3} M_\odot \text{yr}^{-1}$ (Davidson & Humphreys 1997; Davidson et al. 2001; Hillier et al. 2001, 2006; Groh et al. 2012b). A decrease in the observed strength of H α and Fe II emission lines, and a change in the strength of N II lines, provide indications that the primary wind density has decreased, either due to a global reduction in mass loss or to latitudinal changes (e.g., Davidson et al. 2015; Mehner et al. 2012, 2010b). However, there is contradictory evidence from analysis

of the X-ray light curves (e.g., Madura et al. 2013) and the near constancy of He II $0.4686 \mu\text{m}$ (e.g., Teodoro et al. 2016), which indicate much smaller changes in the mass-loss rate.

The distance of η Car is ~ 2.35 kpc (Allen & Hillier 1993; Davidson & Humphreys 1997; Smith 2006). It is surrounded by the spectacular bipolar Homunculus nebula. The inclination of the polar axis of the Homunculus nebula with the line-of-sight is $\sim 41^\circ$ (Davidson et al. 2001; Smith 2006), and the position angle (PA) of the projected Homunculus axis is $\sim 132^\circ$ (Davidson & Humphreys 1997; Davidson et al. 2001; Smith 2006).

Using ESO's Very Large Telescope Interferometer (VLTI), the diameter of η Car's wind region was measured to be about 5 mas (50% encircled-intensity diameter measured in the field-of-view, FOV, of 70 mas) in the K-band continuum (van Boekel et al. 2003; Kervella 2007; Weigelt et al. 2007). The measured visibilities are in good agreement with the predictions from the detailed spectroscopic model by Hillier & Miller (1998) and Hillier et al. (2001, 2006). A good agreement between the Hillier model and interferometric observations of the LBV P Cyg was reported by Richardson et al. (2013).

First spectro-interferometric VLTI-AMBER observations of η Car (Weigelt et al. 2007) with medium and high spectral reso-

[★] Based on observations collected at the European Organisation for Astronomical Research in the Southern Hemisphere under ESO program 092.D-0289(A).

^{★★} The images in Fig. 4 are available in electronic form at the CDS via anonymous ftp to cdsarc.u-strasbg.fr (130.79.128.5) or via <http://cdsweb.u-strasbg.fr/cgi-bin/qcat?J/A+A/>

lution in the He I 2.059 μm and the Br γ 2.166 μm emission lines allowed us to study the spatial structure of η Car's wind as a function of wavelength with a high spatial resolution of ~ 5 mas and spectral resolutions of 1500 and 12 000. The measured line visibilities agree with predictions of the radiative transfer model of Hillier et al. (2001). We derived 50% encircled-intensity diameters of 4.2 mas (9.9 au), 6.5 mas (15.3 au), and 9.6 mas (22.6 au) in the 2.17 μm continuum, the He I 2.059 μm , and the Br γ 2.166 μm emission lines, respectively (for comparison, the radius R_* of the primary star of η Car is $\sim 100 R_\odot \sim 0.47$ au ~ 0.20 mas; however, R_* is not known well; Hillier et al. 2001).

Smith et al. (2003) studied the stellar light reflected by the Homunculus nebula and found that the velocity of the primary stellar wind is higher near the south pole than at the latitude corresponding to our line-of-sight. Other studies suggest that the spectroscopic and interferometric observations can be explained by the wind-wind collision zone (Groh et al. 2012b; Mehner et al. 2012).

Studies of the binary or binary wind-wind collision zone were reported by many authors (e.g., Damineli 1996; Damineli et al. 1997, 1998, 2000, 2008b; Davidson 1997; Davidson et al. 2005, 2015; Smith & Gehrz 2000; Smith et al. 2004; Smith 2010; Pittard & Corcoran 2002; Corcoran et al. 1997, 2001; Corcoran 2005; Ishibashi et al. 1999; Soker 2003, 2007; Weis et al. 2005; Gull et al. 2006, 2009, 2011, 2016; Nielsen et al. 2007; Weigelt et al. 2007; Kashi & Soker 2007, 2009a,b; Parkin et al. 2009; Groh et al. 2010, 2012b,a; Madura & Owocki 2010; Madura et al. 2012, 2013; Mehner et al. 2010a, 2011, 2012, 2015; Richardson et al. 2010; Teodoro et al. 2013, 2016; Clementel et al. 2015a,b; Hamaguchi et al. 2016). The X-rays are believed to arise from a collision between the winds from the LBV and a hotter O or WR-type star. The CHANDRA X-ray spectrum can be explained (Pittard & Corcoran 2002) by the collision of the primary star wind ($\dot{M} = 2.5 \times 10^{-4} M_\odot \text{yr}^{-1}$, terminal velocity ~ 500 km s $^{-1}$) and the wind of a hot companion ($\dot{M} = 10^{-5} M_\odot \text{yr}^{-1}$, terminal velocity ~ 3000 km s $^{-1}$; probably an extreme Of or a WR star perhaps similar to the three luminous WNLh stars seen elsewhere in the Carina Nebula).

The wind collision leads to a wind-wind collision cavity (e.g., Pittard & Corcoran 2002; Humphreys et al. 2008; Okazaki et al. 2008; Parkin et al. 2009, 2011; Gull et al. 2009, 2011; Madura & Owocki 2010; Madura et al. 2012, 2013; Groh et al. 2010, 2012a,b). Radiative transfer models of the wind-wind collision zone were reported by Clementel et al. (2015a,b). Three-dimensional (3D) smoothed particle hydrodynamic simulations were used to determine the orientation of the binary's orbit (semimajor axis length ~ 15.4 au) in space and on the sky (e.g., Okazaki et al. 2008; Madura et al. 2012). Madura et al. (2012) derived an orbit inclination of 130 to 145° and a PA of the orbital axis projected on the sky of 302 to 327°. Therefore, the orbital axis of the binary is closely aligned with the Homunculus system axis. The argument of periaapsis places the secondary star and wind-wind collision zone on the observer's side of the system when the companion star is at apastron.

Detailed HST/STIS imaging of η Car with a resolution of about 0.1'' allowed Gull et al. (2009, 2011), Mehner et al. (2010a), Teodoro et al. (2013), and Gull et al. (2016) to image the circumstellar environment of η Car across emission lines and at several orbital phases. The discovered structures are the result of the wind-wind collision over the past ~ 20 yr. These structures are called fossil wind structures, because they were created over several orbital cycles in the past.

Various observations suggest that disk-like or toroidal material in our line-of-sight to the central object partially obscures

Table 1. Summary of observations

Date	N_{obs}^a	N_{vis}^b	Cal
2013 Dec 31	1	2	HD92305
2014 Jan 04	1	3	HD28749
2014 Jan 19	2	1	HD18660
2014 Jan 20	9	5	HD23319
2014 Jan 21	10	0	-
2014 Feb 03	1	0	-
2014 Feb 06	1	0	-
2014 Feb 07	1	0	-
2014 Feb 08	1	0	-
2014 Feb 09	1	0	-
2014 Feb 13	1	0	-
2014 Feb 14	1	0	-
2014 Feb 21	2	0	-
2014 Feb 22	3	0	-
2014 Feb 23	1	0	-
2014 Feb 24	1	0	-
2014 Feb 25	1	0	-
2014 Feb 26	2	0	-
2014 Feb 27	3	0	-
2014 Feb 28	2	0	-
2014 Mar 04	2	0	-
2014 Mar 05	3	3	HD46933

Notes.^a Number of observations at different hour angles per night.
^b Number of visibilities calibrated with an interferometric calibrator star.

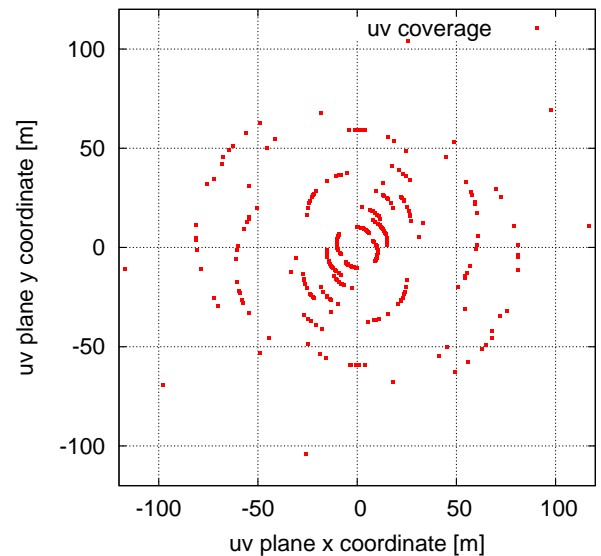


Fig. 1. uv coverage of all VLTI/AMBER observations listed in Table 1.

the central star (e.g., Hillier & Allen 1992; Weigelt et al. 1995; Davidson et al. 1995, 1997; Hillier et al. 2001; Smith et al. 2002, 2004; Mehner et al. 2010a; Madura et al. 2013). To study this occulting material, Falcke et al. (1996) performed speckle masking imaging polarimetry (in H α plus continuum). The polarized flux image (Fig. 2b in the polarimetry paper) shows a bar with a length of $\sim 0.4''$ along a PA of ~ 45 and 225° , which was interpreted as an obscuring equatorial disk. Interestingly, this polarized 45° bar has approximately the same length and PA as the fossil wind bar discovered by Gull et al. (2011, 2016).

In this paper, we present high spatial and high spectral resolution aperture-synthesis imaging of η Car's innermost wind region. We describe the observations in Section 2, while in Section 3, we present the velocity-resolved aperture-synthesis images re-

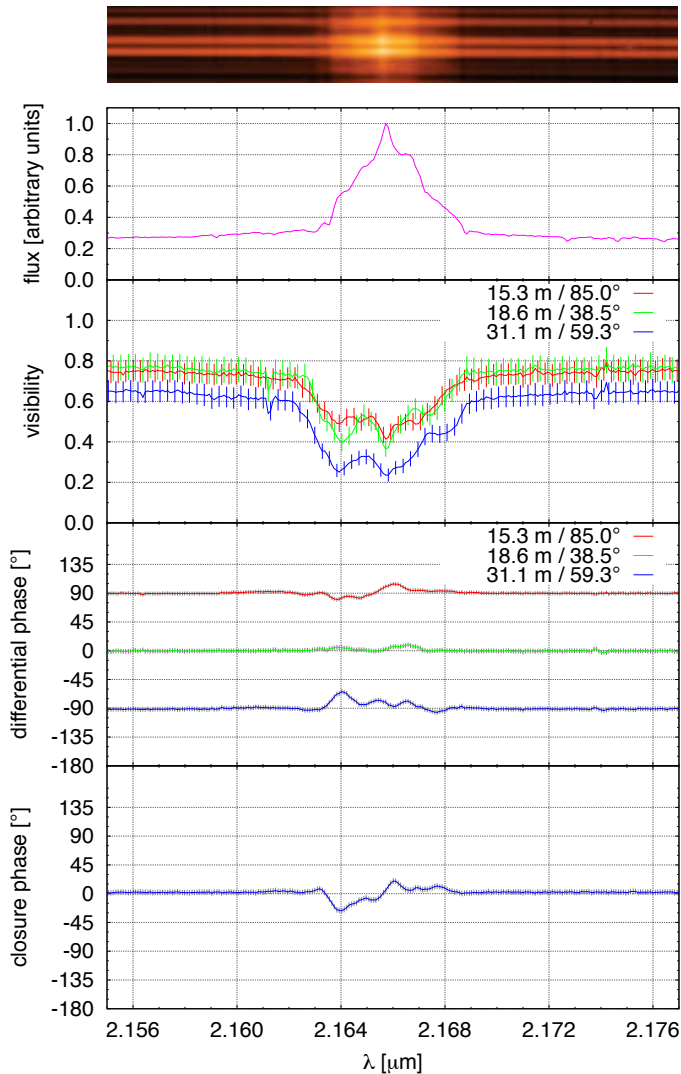


Fig. 2. Illustrative example of an AMBER HR-mode ($R = 12\,000$) observation of η Car (see Sect. 2). The figure shows from top to bottom: example interferogram, spectrum of the Br γ region (heliocentric wavelengths; the telluric lines are not removed), wavelength dependence of the visibilities at three baselines (PAs and projected baseline lengths are indicated in the panels), wavelength-differential phases (the curve of the shortest baseline is shifted up by 90° and the longest down by 90°), and closure phases.

constructed from the VLTI data. All images show the extended wind region, which is more extended across the Br γ line than in the continuum. In Section 4, we discuss the results. Section 5 is a summary and conclusion.

2. Observations and data processing

2.1. Visibilities, wavelength-differential phases, and closure phases

The observations of η Car listed in Table 1 were carried out with the ESO Very Large Telescope Interferometer (VLTI; Schöller 2007) and the AMBER interferometry instrument (Petrov et al. 2007). With projected baseline lengths up to about 129 m of the Auxiliary 1.8 m Telescopes (ATs) used, an angular resolution of ~ 6 mas (~ 14 au) was obtained in the K band. Interferograms were recorded with the high spectral resolution mode (HR mode; spectral resolution $R = 12\,000$). Figure 1 shows the uv coverage

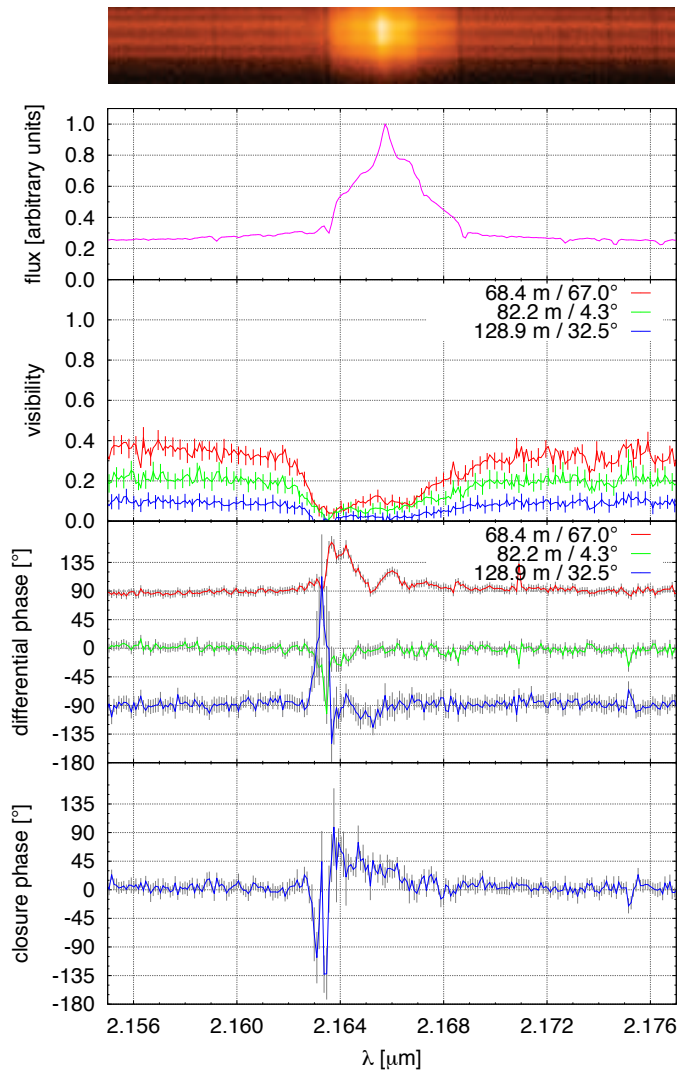


Fig. 3. Same as Fig. 2, but different telescope configuration.

of the observations. The spatial-filter fibers in AMBER limit the FOV to the diameter of the fibers on the sky (~ 250 mas for the ATs). The observations were carried out as part of the OHANA (Rivinius et al. 2015) backup target project (Observatory survey at High ANgular resolution of Active OB stars; Prog-ID: 092.D-0289).

Figures 2 and 3 present two examples of high spectral resolution η Car AMBER observations (the dates of observations shown in Figs. 2 and 3 are 20 January 2014, 8:15 UT and 4 January 2014, 5:31 UT, respectively). The figures show, from top to bottom, an example of an AMBER interferogram, the line profile, the visibilities obtained at three different baselines as a function of wavelength, the wavelength-differential phases at three baselines, and the wavelength dependence of the closure phase. For the observations, the FINITO fringe tracker (Le Bouquin et al. 2008) was employed. The observations were obtained between seven and five months before the 2014.6 periastron passage (see Table 1). The observing dates correspond to an average orbital phase of ~ 0.90 if calculated as described in Mehner et al. (2011) and 0.91 if calculated as described in Damineli et al. (2008b) or Teodoro et al. (2016).

We analyzed whether the interferometric observables (spectrum, visibilities, and phases of the object Fourier transform) changed over the two-month-long observing interval and found

negligible changes. Therefore, all observations were combined to compute an averaged image. While the orbital eccentricity is ~ 0.90 (Corcoran et al. 2001; Pittard & Corcoran 2002), the change in position of the companion relative to the primary star is small and the temporal evolution of the cavity is expected to be small over the observing interval. The latter is substantiated by small changes in 3-D hydrodynamic models of the wind-wind cavity that were computed at orbital phases 0.50, 0.90, and 0.952 (Madura et al. 2012, 2013).

The data were reduced with our own AMBER data processing software package, which uses the pixel-to-visibility matrix algorithm P2VM (Tatulli et al. 2007; Chelli et al. 2009) in order to extract visibilities, differential phases, and closure phases for each spectral channel of an AMBER interferogram. We derived 50 wavelength-dependent closure phases and 150 wavelength-differential phases from the interferograms. For only 14 of the observations are suitable calibrator star measurements available to calibrate the interferometric transfer function and the visibilities (see Table 1). The number of calibrator measurements is small because the data were recorded within a backup-target programme (Prog-ID: 092.D-0289). The wavelength calibration was performed using telluric lines. We used the same method as described in Appendix A of Weigelt et al. (2007).

The performance of the fringe tracker FINITO is usually different during target and calibrator observations, because the performance of FINITO depends on atmospheric conditions, target brightness, and target visibility. This can lead to visibility calibrations of low quality. Therefore, we used the VLTI Reflective Memory Network Recorder (RMNrec) data (Le Bouquin et al. 2009; Mérand et al. 2012) to improve the visibility calibration by rejecting 46% of the exposures that showed a disagreement between the RMNrec values of calibrator and science object.

The calibrated continuum visibilities were fit with a two-dimensional exponential function in Fourier space, because the measured visibilities and the Fourier transform of the Hillier continuum model curves are approximately exponential functions (van Boekel et al. 2003; Kervella 2007; Weigelt et al. 2007). From this visibility, we derived an axis ratio of 1.07 ± 0.14 and a PA of the major axis of $159.5 \pm 47^\circ$. The axis ratio and the PA are not well constrained because the visibility errors are large and the number of calibrated visibilities is small. This model visibility function was used to calibrate the visibilities of the observations made without a calibrator (see Table 1).

2.2. Differential-phase and closure-phase image reconstruction methods

We used two different image reconstruction methods, called below differential-phase method and closure-phase method. If spectrally dispersed interferograms are available, the wavelength-differential phases in spectral channels across emission lines can be used to derive phases of the Fourier transform of the object in spectral channels across emission lines (Petrov et al. 2007; Schmitt et al. 2009; Millour et al. 2011; Ohnaka et al. 2011, 2013; Mourard et al. 2015). This is possible if the phase of the Fourier transform of the object in the continuum is known (for example, if the continuum object is unresolvable) or can be derived from a continuum image reconstructed from continuum visibilities and continuum closure phases using a closure phase method. The reconstruction of images from a set of visibilities and phases of the object Fourier transforms derived from differential phases is discussed in Appendix A. This method is called differential-phase method in the following sections. To reconstruct images using the differential-phase method,

we used the minimization algorithm ASA-CG (Hager & Zhang 2006), as described in (Hofmann et al. 2014). The images presented in Figs. 4, 5, 6, B.1, and B.2 were reconstructed with this differential-phase method.

Alternatively, we can reconstruct images from visibilities and closure phases (Jennison 1958). This method is briefly called closure-phase method in the following sections. We used the *IR-Bis* method (Infrared Bispectrum image reconstruction method) for image reconstruction (Hofmann et al. 2014). The images presented in Fig. A.1 in Appendix A were reconstructed with the closure-phase method. Data processing is discussed in Appendix A in more detail.

3. Velocity-resolved aperture-synthesis images of η Car's stellar wind and wind-wind collision zone across the Br γ line

We reconstructed images with both methods (differential- and closure-phase method) discussed in Sect. 2. Both methods were used to illustrate the similarities and differences of the reconstructions.

Figure 4 presents the images reconstructed from the observations listed in Table 1 using the differential-phase method (Sect. 2). The images clearly show a strong wavelength dependence across the Br γ line. One of the most remarkable features of the images is the fan-shaped structure extending to the south-east (SE; from PA $\sim 90^\circ$ to $\sim 180^\circ$) at velocities between approximately -376 and -140 km s $^{-1}$. Figure 5 shows the image at -277 km s $^{-1}$ to illustrate the asymmetric, fan-shaped structure and its size. As we will discuss in the next section, the size, structure, and velocity dependence of these images suggest that we have obtained the first direct images of the walls of the wind-wind collision cavity. Another interesting and unexpected structure is the bar-like structure that extends to the southwest (SW) in the images at velocities from -426 to -339 km s $^{-1}$.

The images presented in Fig. A.1 in Appendix A were reconstructed with the closure-phase method (see Sect. 2). For the reconstructions in Fig. A.1, we used the same data set as for the reconstructions shown in Fig. 4.

Figures 4 to 6 present images that consist of both continuum and Br γ line components. To assist in the interpretation of the Br γ line images, we additionally computed the continuum-subtracted Br γ line images shown in Figs. B.1 and B.2 in Appendix B (these two figures show images of different velocity ranges). The white crosses are the centers of the continuum images. The images reconstructed with the differential-phase method (Fig. 4) seem to have a slightly higher signal-to-noise ratio than the closure-phase images (Fig. A.1) because of the larger amount of Fourier phase information (i.e., 150 Fourier phases instead of 50 closure phases). Therefore, the differential-phase images were used to compute all continuum-subtracted Br γ line images.

The continuum-subtracted images in Figs. B.1 and B.2 show the correct Br γ brightness of the images, because they are not normalized to the peak brightness as the images in all previous figures. The computation of the continuum-subtracted images is discussed in Appendix B.

Surprisingly, in the continuum-subtracted images at highest negative velocities (≤ -563 km s $^{-1}$) in Fig. B.1, the center of the Br γ line emitting region is clearly shifted about 1–2 mas to the northwest (NW) of the center of the continuum image. To study this unexpected offset in more detail, we computed the continuum-subtracted images shown in Fig. B.2 (wider ve-

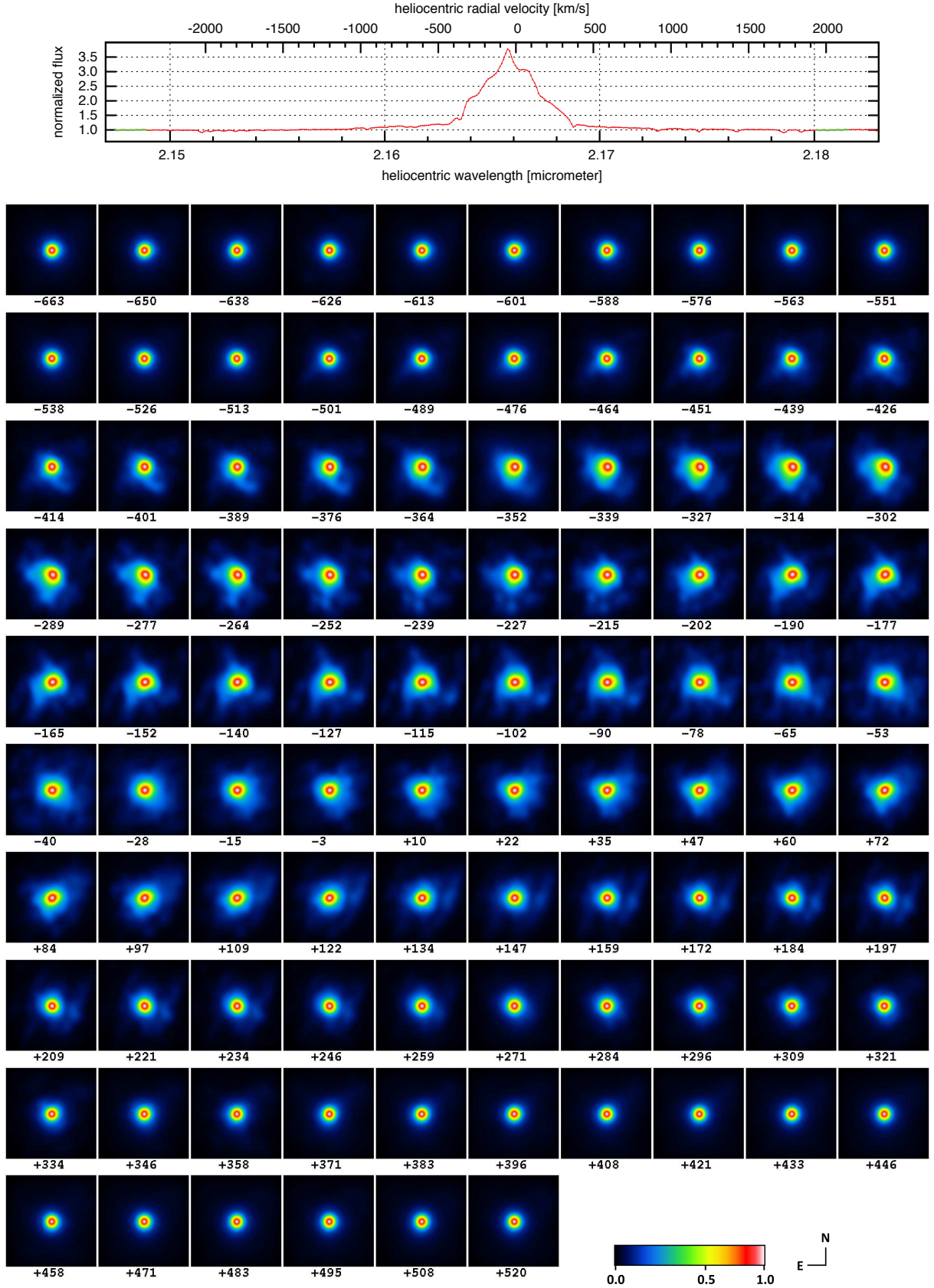


Fig. 4. Aperture-synthesis images of η Car reconstructed with the differential-phase method (see Sect. 2; spectral resolution $R = 12\,000$). *Top:* Continuum-normalized Br γ line profile. The presented spectrum is the average of all spectra of the data listed in Table 1. The small correction due to the system velocity of -8 km s^{-1} (Smith 2004) has been neglected. *Bottom:* Wavelength and velocity dependence (velocities in units of km s^{-1} below the images) of the reconstructed η Car images across the Br γ line. The FOV of the reconstructed images is $50 \times 50\text{ mas}$ ($118 \times 118\text{ au}$; 1 mas corresponds to 2.35 au). North is up, and east is to the left. In all images, the peak brightness is normalized to unity. At radial velocities between approximately -339 and -252 km s^{-1} , the images are *fan-shaped* and extended to the SE of the center of the continuum wind region.

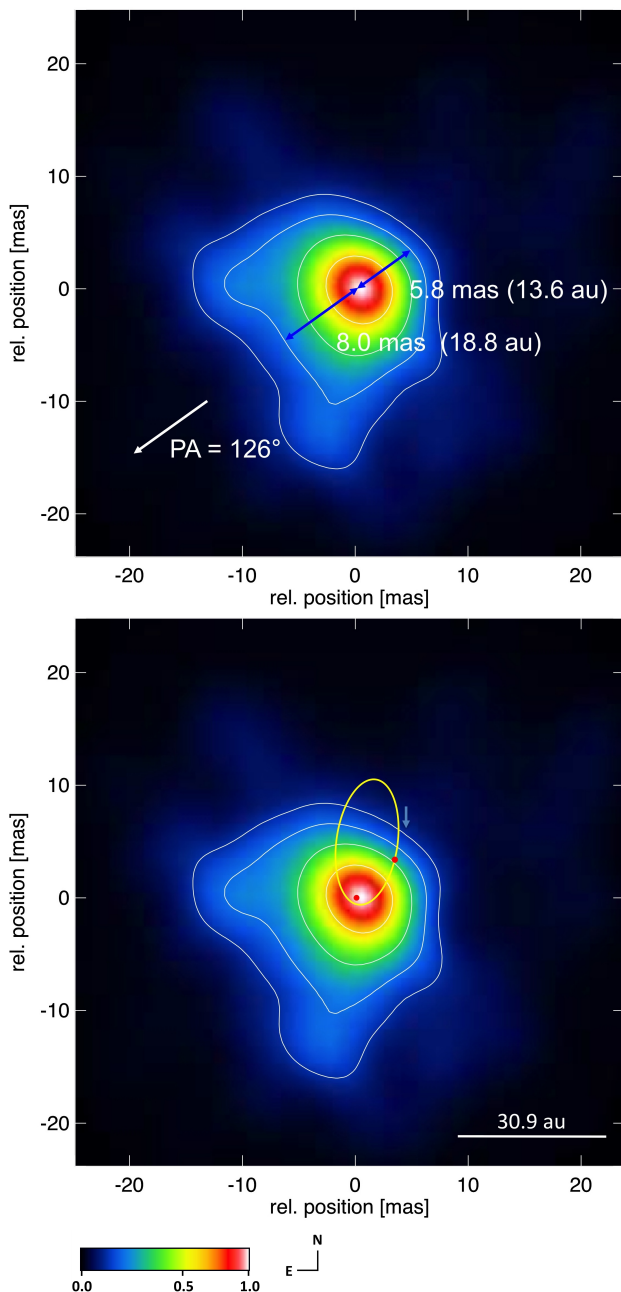


Fig. 5. *Top:* Fan-shaped η Car image at velocity of -277 km s^{-1} (image from Fig. 4). The FOV of the image is $50 \times 50 \text{ mas}$ ($118 \times 118 \text{ au}$; the center of the continuum region is at coordinate zero). Contour lines are plotted at 8, 16, 32, and 64% of the peak intensity. The PA of the symmetry axis of the fan is $\sim 126^\circ$ (white arrow). The fan-shaped structure extends $\sim 18.8 \text{ au}$ (8.0 mas; blue arrow) to the SE and $\sim 13.6 \text{ au}$ (5.8 mas) to the NW, measured with respect to the center of the continuum wind along the fan symmetry axis at the 16% intensity contour. For comparison, the radius R_* of the primary star of η Car is $\sim 100 R_\odot \sim 0.47 \text{ au} \sim 0.20 \text{ mas}$ (R_* is not well known; Hillier et al. 2001). Therefore, the huge wind extension to the SE is about 40 times larger than R_* . *Bottom:* Overlay of a sketch of the orbit of the secondary star relative to the primary star on the sky (yellow) and the fan-shaped image at -277 km s^{-1} . The orbit is adopted from Teodoro et al. 2016 (phase 0.91 computed as described in this paper). The two red dots are the primary and the secondary star at the time of our observations. The binary separation and PA were approximately 4.9 mas (11.5 au) and 315° , respectively, at the time of observation (Sect. 4). The blue arrow indicates the motion direction and the bar at the bottom right the length of the major axis of the orbit (30.9 au; Madura et al. 2012).

locity range) in addition to the continuum-subtracted images in Fig. B.1 (notice the different color code required because of the faintness of most of the images).

The differential-phase (Fig. 4) and closure-phase (Fig. A.1) images are similar, but there are also differences. Both types of images present the discussed fan-shaped wind structure. To show the differences, we derived contour plot images of the differential-phase and closure-phase images at velocities between -376 and -277 km s^{-1} shown in Fig. C.1 in Appendix C.

Figure D.1 in Appendix D presents the velocity dependence of the photocenter shift of the images shown in Fig. 4 (i.e., continuum plus line flux images) with respect to the center of the continuum images. Figure D.2 shows both the velocity dependence of the size of the images in Fig. 4 (measured as 50% encircled-intensity radius) and the velocity dependence of the photocenter shift of the images in Fig. 4 with respect to the center of the continuum images. The biggest photocenter shifts are caused by the fan-shaped structure seen at many high negative velocities.

In Appendix E, we compare the measured visibilities, differential phases, and closure phases shown in Figs. 2 and 3 with the visibilities and phases derived from the images reconstructed with the differential-phase method to check whether the interferometric quantities of the reconstructed images approximately agree with the observations.

4. Discussion

The reconstructed images in Fig. 4 show a strong wavelength dependence of the intensity distribution across the Bry line.

- At wavelengths corresponding to radial velocities lower than about -426 km s^{-1} and higher than about $+400 \text{ km s}^{-1}$, the continuum wind region is dominant.
- At velocities between approximately -426 and -339 km s^{-1} , a bar-like extension appears in the southwest (SW) of the continuum wind.
- Between approximately -376 and -140 km s^{-1} , a fan-shaped structure is visible in the SE of the continuum wind. This unexpected fan-shaped structure is discussed in Figs. 5 and 6 in more detail.
- The wind intensity distribution is more extended at most high negative velocities (e.g., -350 to -250 km s^{-1}) than at high positive velocities (e.g., $+250$ to $+350 \text{ km s}^{-1}$).
- At all velocities, the continuum wind region is shining through the Bry emitting wind region, suggesting that the line-emitting region is optically thin.
- The continuum-subtracted images in Figs. B.1 and B.2 show that a faint line-emitting region is visible at high negative and positive velocities. At some high negative velocities (e.g., about -563 to -825 km s^{-1} in Fig. B.2), the center of the line emission is offset to the NW of the center of the continuum wind (see Sect. 4.1).

Figure 5 illustrates the geometry of the fan-shaped image at -277 km s^{-1} . Figure 6 (second row) has the goal to highlight the evolution of the fan-shaped structure between -364 and -277 km s^{-1} and (third row) compare images obtained at negative and positive velocities to illustrate the structure and size differences. For example, the images at velocities of -277 and $+271 \text{ km s}^{-1}$ clearly show a big size difference. This comparison and the cavity model sketch at the bottom of Fig. 6 are needed in the following discussions.

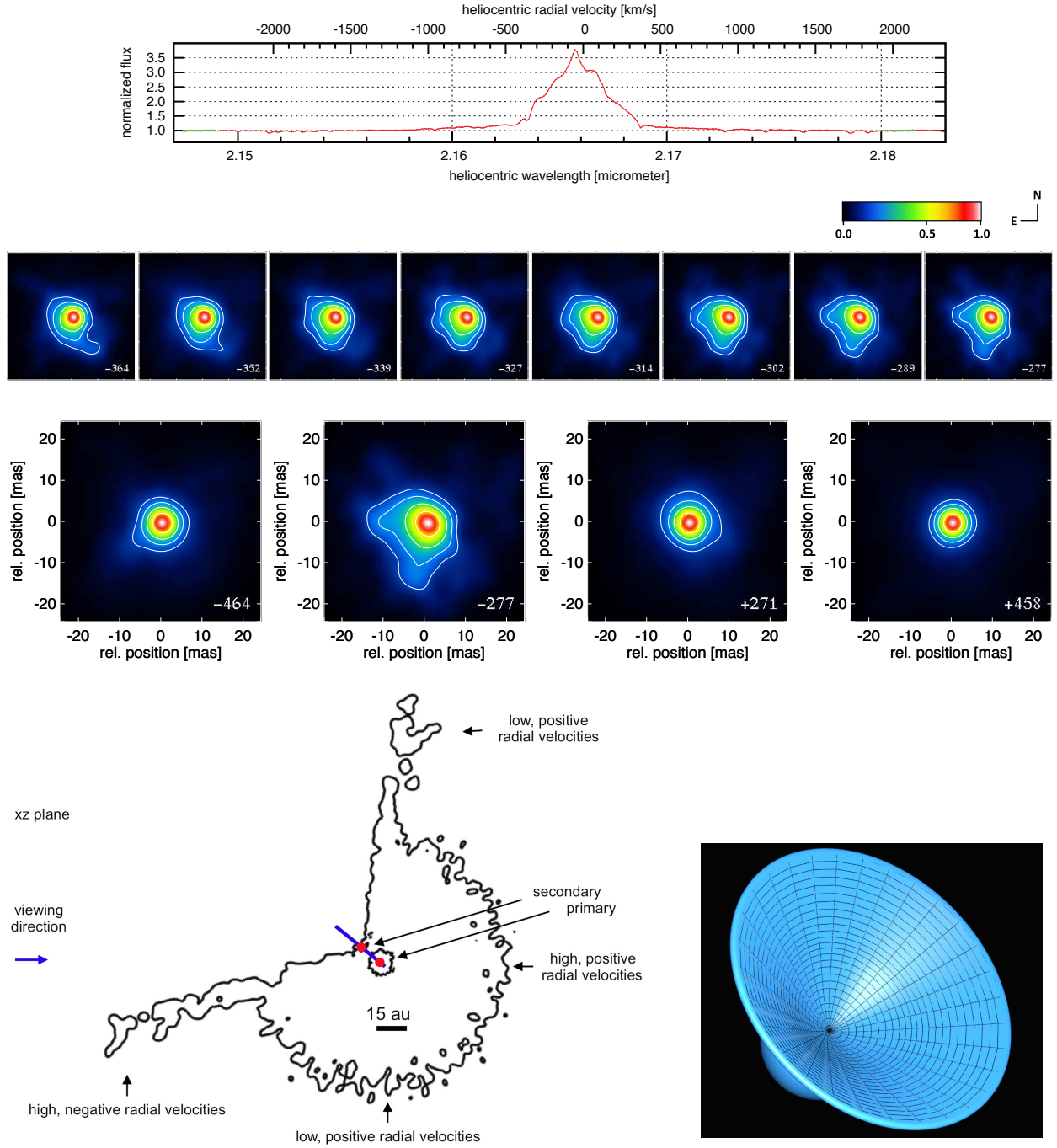


Fig. 6. Comparison of η Car images with model density distributions. *Top:* Continuum-normalized Bry line profile (same as in Fig. 4). *Second row:* SW bar structure at velocities of -364 to -352 km s^{-1} and fan-shaped SE structure at velocities of about -339 to -277 km s^{-1} (images from Fig. 4; the FOV is 50×50 mas or 118×118 au; 1 mas corresponds to 2.35 au; north is up, and east is to the left). Contour lines are plotted at 8, 16, 32, and 64% of the peak intensity. The fan-shaped SE structures suggest that the reconstructed images are direct images of the wind-wind collision zone. *Third row:* From left to right, images at velocities of -464 km s^{-1} (continuum), -277 km s^{-1} (fan-shaped SE extension), $+271$ km s^{-1} , and $+458$ km s^{-1} (continuum). At velocity of -277 km s^{-1} , the image is asymmetric, fan-shaped, and more extended than the image at velocity of $+271$ km s^{-1} . *Bottom left:* Illustration of the V-shaped wind-wind collision model, our viewing direction at the time of observation, and the radial velocities seen by the observer. The iso-density contours are extracted from the model presented in Fig. B1 (phase 0.90) in Madura et al. (2013). Two density contours (10^{-16} g cm^{-3} and 10^{-14} g cm^{-3}) of the model density distribution are shown. The binary orbit (semimajor axis length ~ 15.45 au) is sketched as a blue line. The projected elliptical orbit is a line in the shown plane perpendicular to the orbital plane (Madura et al. 2012, 2013). The two red dots mark the positions of the primary and secondary star at the time of observation (binary separation ~ 4.9 mas or 11.5 au; see Sect. 4). *Bottom right:* Line-of-sight view of a three-dimensional iso-density surface (density 10^{-16} g cm^{-3}) of the wind at the time of observation (north is up, and east is to the left; FOV is $\sim 50 \times 50$ mas). This iso-density distribution is a smoothed version of model iso-density derived by Madura et al. (2013). A small part of the Bry primary wind is visible to the SE. The continuum primary wind is not visible because its diameter is smaller than the Bry primary wind. The binary separation and PA were approximately 4.9 mas (11.5 au) and 315° , respectively, at the time of observation. The secondary star is not visible in the images, because it is at least about 100 times fainter than the primary star, which is also not visible due to high extinction.

At velocity of -277 km s^{-1} , the reconstructed image has a fan-shaped intensity distribution (see Fig. 5). The PA of the symmetry axis of the fan is $\sim 126^\circ$. The fan-shaped structure extends $\sim 8.0 \text{ mas}$ (18.8 au) to the SE along a PA of $\sim 126^\circ$ and $\sim 5.8 \text{ mas}$ (13.6 au) to the NW along a PA of $\sim 306^\circ$ measured with respect to the center of the continuum wind image at the 16% intensity contour.

The observed image asymmetries indicate that *the LBV wind is not spherical or that there is an external influence on the wind*. For the discussions in the next sections, we need to know the position of the secondary star on the sky at the time of observation. The 3-D orientation of η Car's orbit was derived by Madura et al. (2012). Using these results and assuming the latest orientation parameters and orbit, as shown in Fig. 17 in Teodoro et al. (2016), we derived the projected binary separation of approximately 4.9 mas (11.5 au) and PA of 315° at the time of observation. The secondary star is not visible in our images, because it is at least about 100 times fainter than the primary star (e.g., Hillier et al. 2006; Weigelt et al. 2007). The primary is also not visible due to high extinction.

In the next sections, we discuss the high-velocity gas (Sect. 4.1), the toroidal gas (Sect. 4.2), the fossil wind (Sect. 4.3), the polar wind (Sect. 4.4), and the wind-wind collision (Sect. 4.5), because all of them may influence the observed images.

4.1. High-velocity structure in the continuum-subtracted images

In the continuum-subtracted images presented in Fig. B.2, the center of most of the $\text{Br}\gamma$ line images is at the center of the continuum images (marked by white crosses). However, in the velocity range of about -613 to -825 km s^{-1} , the center of the $\text{Br}\gamma$ line emitting region is clearly shifted about $1\text{--}2 \text{ mas}$ to the NW of the center of the continuum image. At -663 km s^{-1} , the NW offset is $1.7 \pm 0.4 \text{ mas}$ along a PA of $292 \pm 20^\circ$. At velocities smaller than about -837 km s^{-1} , the high-velocity structure is still visible, but the NW offset disappeared.

In the $\text{Br}\gamma$ line profile, the outer high-velocity region is dominated by the electron scattering wings (e.g., Hillier et al. 2001; Groh et al. 2010). However, in the blue line wing, there may also be additional line contributions from (1) fast moving primary wind gas (in the wind cavity) accelerated by the fast secondary wind (Damineli et al. 2008a; Groh et al. 2010), and (2) the weak $\text{He I } 2.16127 \mu\text{m}$ line (the center of this line is approximately at velocity of about -550 km s^{-1} in the $\text{Br}\gamma$ line profile). Model spectra of η Car computed with the radiative transfer model of Hillier & Miller (1998) and Hillier et al. (2001) show that the peak brightness of this $\text{He I } 2.16127 \mu\text{m}$ line is about 50 to 100 times weaker than the peak brightness of the $\text{Br}\gamma$ line.

The cause of the observed $\sim 1\text{--}2 \text{ mas}$ ($2.35\text{--}4.7 \text{ au}$) NW offset of the line images at about -613 to -825 km s^{-1} is unknown, but the high negative velocity and location of the high-velocity structure suggest that the emitting region (of both the above discussed high-velocity $\text{Br}\gamma$ emission and the $\text{He I } 2.16127 \mu\text{m}$ emission) is located in the innermost region of the wind-wind collision cavity (Damineli et al. 2008a; Groh et al. 2010), because the innermost region of the cavity was in the NW of the center of the continuum image at the phase of our observations (binary separation and PA were 4.9 mas or 11.5 au and 315° at the time of observation).

4.2. Toroidal occulting gas and dust in the line-of-sight to the central object

Occulting gas in the line-of-sight to the central object may influence the observed intensity distributions for the following reasons. The three ejected objects η Car B, C, and D at separations between $0.1''$ (235 au) and $0.3''$ (Weigelt & Ebersberger 1986; Hofmann & Weigelt 1988) were only about 12 times fainter than the central object in 1985 at the wavelength of about 900 nm . In the UV (at $\sim 190 \text{ nm}$), where obscuring material leads to much more extinction, these objects B to D were only about three times fainter than the central object in 1991 (Weigelt et al. 1995).

This seems to be puzzling because the objects B, C, and D are objects illuminated by the central object (and only a very small fraction of the star flux hits these objects). Therefore, several authors suggested that disk-like or toroidal occulting material in our line-of-sight to the central object may partially obscure the central star, but not the objects B, C, and D, just like a natural coronagraph (Hillier & Allen 1992; Weigelt et al. 1995; Davidson et al. 1995, 1997; Hillier et al. 2001; Smith et al. 2002, 2004; Mehner et al. 2010a; Madura et al. 2013).

To study this occulting toroidal material, Falcke et al. (1996) performed speckle masking imaging polarimetry in the $\text{H}\alpha$ line. The image obtained in polarized light (see Fig. 2b in the polarimetry paper) shows a bar with a length of $\sim 0.4''$ (940 au) along a PA of $\sim 45^\circ$ and $\sim 225^\circ$ (about equal to the PA of the equatorial plane of the Homunculus). It was interpreted as an obscuring equatorial disk. Interestingly, this polarized bar has approximately the same length and PA as the fossil wind bar discussed in the next section.

Furthermore, in Fig. 4, a bar- or arc-like structure along PA of $\sim 225^\circ$ can be seen at velocities between approximately -426 and -339 km s^{-1} that may be caused by gas in the inner region of the equatorial disk or torus.

4.3. Fossil wind

The bar-like SW extension at PA of $\sim 225^\circ$ in Figs. 4 to 6 and B.1 is mainly visible at velocities between approximately -426 and -339 km s^{-1} . Its PA of $\sim 225^\circ$ approximately agrees with the PA of the fossil wind structure reported by Gull et al. (2011, 2016) and the polarisation bar (Falcke et al. 1996). The images of the fossil wind structure (at $\sim 0.1\text{--}0.5''$) in Gull et al. (2011) were made by integrating the HST/STIS observations over the velocity range of -400 to -200 km s^{-1} (see also the wind studies in Gull et al. 2009; Madura & Owocki 2010; Teodoro et al. 2013). The fossil wind may slightly influence the intensity distribution of the dominant inner wind region. However, the fossil wind is faint compared to the innermost wind-wind collision zone.

Interestingly, both the intensity contours of the blueshifted $\text{Fe III } 0.4659 \mu\text{m}$ HST/STIS map in Mehner et al. (2010a) and the aforementioned blue-wing images in Gull et al. (2011) show a similar asymmetric structure as some of our fan-shaped VLTI images, although of course HST's angular resolution was inferior. Mehner et al. (2010a) discuss various origins of this structure, for example, the near side of a latitude-dependent structure in the outer stellar wind, the inner parts of the Homunculus ejecta, or the obscuring material that causes about two magnitudes more the extinction in front of the primary star than in front of the ejecta at separations between 0.1 and $0.3''$. The fan-shaped images also look like inclined bipolar nebulae with a symmetry axis parallel to the Homunculus axis.

4.4. High-density fast polar wind

In the SE of the continuum center, we are looking at the south polar region of the stellar wind (Smith et al. 2003), because the inclination of the polar axis of the Homunculus nebula with the line-of-sight is $\sim 41^\circ$ (Davidson et al. 2001; Smith 2006) and the PA of the projected Homunculus axis is $\sim 132^\circ$ (Davidson & Humphreys 1997; Davidson et al. 2001; Smith 2006). Smith et al. (2003) studied the stellar light reflected by different regions of the Homunculus nebula and found that the wind velocity and density of the massive primary wind of η Car is higher at the polar region than at latitudes corresponding to our line-of-sight, and the polar wind axis is approximately parallel to the Homunculus axis. Therefore, the SE extension of our images may at least partially be caused by an increased wind density at the south pole. On the other hand, other studies suggest that the spectroscopic and interferometric observations can be explained by the wind-wind collision zone (Groh et al. 2012b; Mehner et al. 2012).

4.5. Wind-wind collision zone

3-D smoothed particle hydrodynamic simulations of η Car's colliding winds predict a bow shock with an enhanced density and an extended wind-wind collision cavity or bore hole (Okazaki et al. 2008; Gull et al. 2009, 2011; Groh et al. 2010; Madura & Owocki 2010; Madura et al. 2012, 2013; Clementel et al. 2015b,a) that has a density distribution *more extended than the undisturbed primary wind region*, as in our observed images. This large extension of the wind-wind collision zone can, for example, be seen in the model density distributions presented in Fig. 18 (see insets) in Gull et al. (2009), Fig. 6 in Madura et al. (2012), Figs. B1 (orange region), 1, and 10 in Madura et al. (2013), Fig. 2 in Clementel et al. (2015b), and in the sketch in Fig. 6.

Because of the orbit orientation in space, the secondary star of η Car spends most of the time in front of the primary star (e.g., Madura et al. 2012, 2013). Only for a few weeks around the periastron passage are the secondary star and the wind-wind collision zone behind the primary star (on the back or far side of the primary wind). According to aforementioned hydrodynamical simulations, at the time of observation, the secondary star was in front of the primary star, and we were looking at the extended wind-wind collision cavity (e.g., Madura et al. 2012). In other words, the wind collision cavity was opened up into our line-of-sight at the time of observation.

Unfortunately, no η Car model images of the Bry intensity distribution (e.g., 3-D smoothed particle hydrodynamic simulations combined with radiative transfer modeling) are available. Therefore, we use the density distribution of 3-D smoothed particle hydrodynamic simulations (see above references) for the following discussion.

Figure 6 (bottom left) illustrates the wind-wind collision cavity and our viewing direction at orbital phase of 0.90. Two density contour lines (density 10^{-16} g cm $^{-3}$ and 10^{-14} g cm $^{-3}$) of the wind collision cavity model presented in Fig. B1 in Madura et al. (2013) are shown (bottom left). The lower arm of the wind-wind collision cavity depicted in the sketch in Fig. 6 (bottom left) can be seen in the reconstructed images (Figs. 4 and 6) to the SE of the center of the continuum wind, given the orientation of the orbit (Madura et al. 2012).

To illustrate the complicated 3-D wind structure, Fig. 6 (bottom right) shows a line-of-sight view of a smoothed three-dimensional iso-density surface (density 10^{-16} g cm $^{-3}$) of the

wind model (Madura et al. 2013) at the time of observation. In the next paragraphs, we will discuss the size and structure of the images at different velocities.

(1) *High positive radial velocities.* At high positive radial velocities, for example +200 to +400 km s $^{-1}$, the observed Bry wind intensity distributions are only slightly wider than the continuum wind region (see Figs. 4, A.1, B.1, and the +271 km s $^{-1}$ image in the third row of Fig. 6). The sketch at the bottom of Fig. 6 illustrates that the emission region corresponding to these high positive radial velocities is predicted to be on the back side of the primary wind (i.e., on the far side behind the primary star) and to have a *smaller angular diameter* than, for example, the emission region with very small radial velocity (e.g., zero). The primary wind on the back side is not disturbed by the wind-wind collision zone at the orbital phase of our observations. We note that in all images in Figs. 4 to 6 and A.1, the peak brightness is normalized to unity. This explains why the compact wind at high positive velocities is not more visible in spite of the high line flux at these wavelengths.

(2) *Low radial velocities.* The sketch in Fig. 6 shows that the model region of small positive radial velocities (marked as "low, positive radial velocities" at the top of the sketch) is the upper cavity region. This upper cavity region is in the NW of the continuum center because of the orientation of the orbit (Madura et al. 2012). This NW extension is only weakly visible in the reconstructed images in Fig. 4 (e.g., at velocities of +22 to +77 km s $^{-1}$). The reason may be the small cross-section of the outer region in our viewing direction (i.e., we are looking through only a small amount of material). However, the faint low-velocity NW extension of the intensity distribution of the wind collision zone is clearly visible in the continuum-subtracted images (see Fig. B.1).

(3) *High negative radial velocities in the range of approximately -140 to -376 km s $^{-1}$.* The sketch in Fig. 6 suggests that the wind collision cavity was opened up into our line-of-sight at the time of observation, and that the emission from the lower arm of the cavity has *high negative radial velocities*. The lower arm is in the SE of the center of the continuum wind because of the orientation of the orbit (Madura et al. 2012). At radial velocities between -215 and -376 km s $^{-1}$, the reconstructed images (Fig. 4) clearly show a fan-shaped SE extension as predicted by the wind-wind collision model (sketch in Fig. 6). This suggests that our images are *direct images of the inner wind-wind collision cavity*. Our observations provide detailed velocity-dependent image structures that can be used to test 3-D hydrodynamical, radiative transfer models of massive interacting winds.

This wind-wind cavity interpretation of our images at negative velocities appears to be more likely than the high-density polar wind interpretation because a high-density polar wind would be expected to show a blue-shifted extension to the SE (near the south pole) and potentially a red-shifted extension to the NW (north pole). Instead we see a blue-shifted extension to the SE (at approximately -140 and -376 km s $^{-1}$) and no red-shifted extension to the NW at similar positive velocities (see Fig. 4). However, we cannot exclude that the additional emission sources discussed in Sect. 4.1 (e.g., the faint He I 2.16127 μ m emission line), the fossil wind, toroidal occulting material in line-of-sight, and a high-density polar wind slightly influence the observed wind cavity intensity distributions.

5. Summary and conclusions

We have presented the first VLTI-AMBER aperture-synthesis images of η Car. The angular resolution of the images is ~ 6 mas (~ 14 au). Velocity-resolved images were obtained in more than 100 different spectral channels distributed across the Br γ 2.166 μ m emission line. The images show that η Car's stellar wind region is strongly wavelength-dependent and asymmetric.

At high negative velocities of -675 to about -825 km s $^{-1}$, the center of the Br γ line emission is located in the NW of the center of the continuum image (offset ~ 1 – 2 mas or 2.35 – 4.7 au; Fig. B.2). The cause of this offset is unknown, but the high negative velocity and location of this high-velocity structure suggest that the emitting region is located in the innermost region of the wind collision cavity (Damineli et al. 2008a; Groh et al. 2010), because both the secondary star and the innermost region of the wind-wind collision cavity were located to the NW of the center of the continuum image at the phase of our observations.

At high positive radial velocities (e.g., $+250$ to $+350$ km s $^{-1}$), the reconstructed Br γ images show a much narrower wind intensity distribution than at high negative radial velocities (e.g., -350 to -250 km s $^{-1}$), because at these positive velocities, we see the back side of the Br γ primary wind behind the primary star. This back-side wind region is less extended than the front-side wind because it is less disturbed by the wind collision zone in front of the primary star.

The images at velocities between approximately -140 and -376 km s $^{-1}$ show a large fan-shaped structure. At velocity of -277 km s $^{-1}$ (see Fig. 5), the PA of the symmetry axis of the fan is $\sim 126^\circ$. The fan-shaped structure extends ~ 8.0 mas (18.8 au) to the SE and ~ 5.8 mas (13.6 au) to the NW, measured along the fan symmetry axis at the 16% intensity contour.

3-D smoothed particle hydrodynamic simulations of η Car's colliding winds predict a large density distribution of the wind-wind collision zone that is more extended than the undisturbed primary wind. At the time of our observations, the secondary star of η Car was in front of the primary star, and the cavity was opened up into our line-of-sight. The observed SE fan-shaped structure at negative radial velocities (Figs. 4 to 6 and B.1) suggests that our reconstructions are *direct images of the wind-wind collision zone*. However, the fossil wind, toroidal occulting material in the line-of-sight, the faint He I 2.16127 μ m emission line, and a high-density polar wind may also slightly influence the observed image intensity distributions. Our observations provide detailed velocity-dependent image structures that can be used to test three-dimensional hydrodynamical, radiative transfer models of massive interacting winds.

Future AMBER, GRAVITY, and MATISSE observations with a better uv coverage combined with 3-D smoothed particle hydrodynamic simulations will provide a unique opportunity to study the wind-wind collision zone of η Car at many different lines in great detail.

Acknowledgements. We thank all ESO colleagues for the excellent collaboration. The telluric spectra used in this work for spectral calibration of the AMBER data were created from data that was kindly made available by the NSO/Kitt Peak Observatory. This publication makes use of the SIMBAD database operated at CDS, Strasbourg, France. We thank the referee for helpful suggestions. AFJM is grateful for financial aid from NSERC (Canada) and FQRNT (Quebec). S.K. acknowledges support from an STFC Rutherford Fellowship (ST/J004030/1) and ERC Starting Grant (Grant Agreement No. 639889). We thank Alexander Kreplin for helpful discussions.

References

Allen, D. A. & Hillier, D. J. 1993, Proceedings of the Astronomical Society of

- Australia, 10, 338
 Chelli, A., Utrera, O. H., & Duvert, G. 2009, A&A, 502, 705
 Clementel, N., Madura, T. I., Kruip, C. J. H., & Paardekooper, J.-P. 2015a, MNRAS, 450, 1388
 Clementel, N., Madura, T. I., Kruip, C. J. H., Paardekooper, J.-P., & Gull, T. R. 2015b, MNRAS, 447, 2445
 Corcoran, M. F. 2005, AJ, 129, 2018
 Corcoran, M. F., Ishibashi, K., Davidson, K., et al. 1997, Nature, 390, 587
 Corcoran, M. F., Ishibashi, K., Swank, J. H., & Petre, R. 2001, ApJ, 547, 1034
 Damineli, A. 1996, ApJ, 460, L49
 Damineli, A., Conti, P. S., & Lopes, D. F. 1997, New Astronomy, 2, 107
 Damineli, A., Hillier, D. J., Corcoran, M. F., et al. 2008a, MNRAS, 386, 2330
 Damineli, A., Hillier, D. J., Corcoran, M. F., et al. 2008b, MNRAS, 384, 1649
 Damineli, A., Kaufer, A., Wolf, B., et al. 2000, ApJ, 528, L101
 Damineli, A., Stahl, O., Kaufer, A., et al. 1998, A&AS, 133, 299
 Davidson, K. 1997, New A, 2, 387
 Davidson, K., Ebbets, D., Johansson, S., et al. 1997, AJ, 113, 335
 Davidson, K., Ebbets, D., Weigelt, G., et al. 1995, AJ, 109, 1784
 Davidson, K. & Humphreys, R. M. 1997, ARA&A, 35, 1
 Davidson, K., Martin, J., Humphreys, R. M., et al. 2005, AJ, 129, 900
 Davidson, K., Mehner, A., Humphreys, R. M., Martin, J. C., & Ishibashi, K. 2015, ApJ, 801, L15
 Davidson, K., Smith, N., Gull, T. R., Ishibashi, K., & Hillier, D. J. 2001, AJ, 121, 1569
 Falcke, H., Davidson, K., Hofmann, K.-H., & Weigelt, G. 1996, A&A, 306, L17
 Groh, J. H., Hillier, D. J., Madura, T. I., & Weigelt, G. 2012a, MNRAS, 423, 1623
 Groh, J. H., Madura, T. I., Hillier, D. J., Kruip, C. J. H., & Weigelt, G. 2012b, ApJ, 759, L2
 Groh, J. H., Nielsen, K. E., Damineli, A., et al. 2010, A&A, 517, A9
 Gull, T. R., Kober, G. V., & Nielsen, K. E. 2006, ApJS, 163, 173
 Gull, T. R., Madura, T. I., Groh, J. H., & Corcoran, M. F. 2011, ApJ, 743, L3
 Gull, T. R., Madura, T. I., Teodoro, M., et al. 2016, ArXiv e-prints [arXiv:1608.06193]
 Gull, T. R., Nielsen, K. E., Corcoran, M. F., et al. 2009, MNRAS, 396, 1308
 Hager, W. & Zhang, H. 2006, SIAM J. Optim., 17, 526
 Hamaguchi, K., Corcoran, M. F., Gull, T. R., et al. 2016, ApJ, 817, 23
 Hillier, D. J. & Allen, D. A. 1992, A&A, 262, 153
 Hillier, D. J., Davidson, K., Ishibashi, K., & Gull, T. 2001, ApJ, 553, 837
 Hillier, D. J., Gull, T., Nielsen, K., et al. 2006, ApJ, 642, 1098
 Hillier, D. J. & Miller, D. L. 1998, ApJ, 496, 407
 Hofmann, K.-H. & Weigelt, G. 1988, A&A, 203, L21
 Hofmann, K.-H. & Weigelt, G. 1993, A&A, 278, 328
 Hofmann, K.-H., Weigelt, G., & Schertl, D. 2014, A&A, 565, A48
 Humphreys, R. M., Davidson, K., & Koppelman, M. 2008, AJ, 135, 1249
 Ishibashi, K., Corcoran, M. F., Davidson, K., et al. 1999, ApJ, 524, 983
 Jennison, R. C. 1958, MNRAS, 118, 276
 Kashi, A. & Soker, N. 2007, MNRAS, 378, 1609
 Kashi, A. & Soker, N. 2009a, New A, 14, 11
 Kashi, A. & Soker, N. 2009b, MNRAS, 397, 1426
 Kervella, P. 2007, A&A, 464, 1045
 Le Bouquin, J.-B., Abuter, R., Bauvir, B., et al. 2008, in Society of Photo-Optical Instrumentation Engineers (SPIE) Conference Series, Vol. 7013, Society of Photo-Optical Instrumentation Engineers (SPIE) Conference Series, 18
 Le Bouquin, J.-B., Abuter, R., Haguenaue, P., et al. 2009, A&A, 493, 747
 Madura, T. I., Gull, T. R., Okazaki, A. T., et al. 2013, MNRAS, 436, 3820
 Madura, T. I., Gull, T. R., Owocki, S. P., et al. 2012, MNRAS, 420, 2064
 Madura, T. I. & Owocki, S. P. 2010, in Revista Mexicana de Astronomía y Astrofísica Conference Series, Vol. 38, Revista Mexicana de Astronomía y Astrofísica Conference Series, 52–53
 Mehner, A., Davidson, K., Ferland, G. J., & Humphreys, R. M. 2010a, ApJ, 710, 729
 Mehner, A., Davidson, K., Humphreys, R. M., et al. 2012, ApJ, 751, 73
 Mehner, A., Davidson, K., Humphreys, R. M., et al. 2010b, ApJ, 717, L22
 Mehner, A., Davidson, K., Humphreys, R. M., et al. 2015, A&A, 578, A122
 Mehner, A., Davidson, K., Martin, J. C., et al. 2011, ApJ, 740, 80
 Mérand, A., Patru, F., Berger, J.-P., Percheron, I., & Poupau, S. 2012, in Proc. SPIE, Vol. 8445, Optical and Infrared Interferometry III, 84451K
 Millour, F., Meilland, A., Chesneau, O., et al. 2011, A&A, 526, A107
 Mourard, D., Monnier, J. D., Meilland, A., et al. 2015, A&A, 577, A51
 Nielsen, K. E., Corcoran, M. F., Gull, T. R., et al. 2007, ApJ, 660, 669
 Ohnaka, K., Hofmann, K.-H., Schertl, D., et al. 2013, A&A, 555, A24
 Ohnaka, K., Weigelt, G., Millour, F., et al. 2011, A&A, 529, A163
 Okazaki, A. T., Owocki, S. P., Russell, C. M. P., & Corcoran, M. F. 2008, MNRAS, 388, L39
 Parkin, E. R., Pittard, J. M., Corcoran, M. F., & Hamaguchi, K. 2011, ApJ, 726, 105
 Parkin, E. R., Pittard, J. M., Corcoran, M. F., Hamaguchi, K., & Stevens, I. R. 2009, MNRAS, 394, 1758
 Petrov, R. G., Malbet, F., Weigelt, G., et al. 2007, A&A, 464, 1

- Pittard, J. M. & Corcoran, M. F. 2002, *A&A*, 383, 636
- Richardson, N. D., Gies, D. R., Henry, T. J., Fernández-Lajús, E., & Okazaki, A. T. 2010, *AJ*, 139, 1534
- Richardson, N. D., Schaefer, G. H., Gies, D. R., et al. 2013, *ApJ*, 769, 118
- Rivinius, T., de Wit, W. J., Demers, Z., & Quirrenbach, A. 2015, in *IAU Symposium*, Vol. 307, *New Windows on Massive Stars*, ed. G. Meynet, C. Georgy, J. Groh, & P. Stee, 297–300
- Schmitt, H. R., Pauls, T. A., Tycner, C., et al. 2009, *ApJ*, 691, 984
- Schöller, M. 2007, *New A Rev.*, 51, 628
- Smith, N. 2004, *MNRAS*, 351, L15
- Smith, N. 2006, *ApJ*, 644, 1151
- Smith, N. 2010, *MNRAS*, 402, 145
- Smith, N., Davidson, K., Gull, T. R., Ishibashi, K., & Hillier, D. J. 2003, *ApJ*, 586, 432
- Smith, N. & Gehrz, R. D. 2000, *ApJ*, 529, L99
- Smith, N., Gehrz, R. D., Hinz, P. M., et al. 2002, *ApJ*, 567, L77
- Smith, N., Morse, J. A., Gull, T. R., et al. 2004, *ApJ*, 605, 405
- Soker, N. 2003, *ApJ*, 597, 513
- Soker, N. 2007, *ApJ*, 661, 482
- Tatulli, E., Millour, F., Chelli, A., et al. 2007, *A&A*, 464, 29
- Teodoro, M., Damineli, A., Heathcote, B., et al. 2016, *ApJ*, 819, 131
- Teodoro, M., Madura, T. I., Gull, T. R., Corcoran, M. F., & Hamaguchi, K. 2013, *ApJ*, 773, L16
- van Boekel, R., Kervella, P., Schöller, M., et al. 2003, *A&A*, 410, L37
- Weigelt, G., Albrecht, R., Barbieri, C., et al. 1995, in *Revista Mexicana de Astronomía y Astrofísica*, vol. 27, Vol. 2, *Revista Mexicana de Astronomía y Astrofísica Conference Series*, ed. V. Niemela, N. Morrell, & A. Feinstein, 11
- Weigelt, G. & Ebersberger, J. 1986, *A&A*, 163, L5
- Weigelt, G., Kraus, S., Driebe, T., et al. 2007, *A&A*, 464, 87
- Weis, K., Stahl, O., Bomans, D. J., et al. 2005, *AJ*, 129, 1694

¹ Max Planck Institute for Radio Astronomy, Auf dem Hügel 69, 53121 Bonn, Germany
e-mail: weigelt@mpifr.de

² South African Astronomical Observatory, PO box 9, 7935, Observatory, South Africa

³ CRESST and X-ray Astrophysics Laboratory, Goddard Space Flight Center, Greenbelt, MD 20771, USA

⁴ Universities Space Research Association, 10211 Wincopin Circle, Suite 500, Columbia, MD 21044, USA

⁵ Instituto de Astronomia, Geofísica e Ciências Atmosféricas, Universidade de São Paulo, Rua do Matão 1226, Cidade Universitária, São Paulo 05508-900, Brazil

⁶ European Southern Observatory, Casilla 19001, Santiago 19, Chile

⁷ I. Physikalisches Institut, Universität zu Köln, Zùlpicher Strasse 77, 50937 Köln, Germany

⁸ School of Physics, Trinity College Dublin, The University of Dublin, Dublin 2, Ireland

⁹ Code 667, Astrophysics Science Division, Goddard Space Flight Center, Greenbelt, MD 20771 USA

¹⁰ Department of Physics and Astronomy & Pittsburgh Particle Physics, Astrophysics, and Cosmology Center (PITT PACC), University of Pittsburgh, 3941 O'Hara Street, Pittsburgh, PA 15260, USA

¹¹ European Southern Observatory, Karl Schwarzschild Strasse 2, 85748 Garching, Germany

¹² University of Exeter, Astrophysics Group, Stocker Road, Exeter, EX4 4QL, UK

¹³ Laboratoire Lagrange, UMR7293, Université de Nice Sophia-Antipolis, CNRS, Observatoire de la Côte d'Azur, 06300 Nice, France

¹⁴ Département de physique and Centre de Recherche en Astrophysique du Québec (CRAQ), Université de Montréal, CP 6128 Succ. A., Centre-Ville, Montréal, Québec H3C 3J7, Canada

¹⁵ Universidad Católica del Norte, Instituto de Astronomía, Avenida Angamos 0610, Antofagasta, Chile

¹⁶ Osservatorio Astrofisico di Arcetri, 5 Largo Enrico Fermi, 50125, Firenze, Italia

¹⁷ Indian Institute of Astrophysics, Koramangala, Bengaluru 560034, India

¹⁸ Ritter Observatory, Department of Physics and Astronomy, The University of Toledo, Toledo, OH 43606-3390, USA

Appendix A: Image reconstruction

The goal of most image reconstruction methods is to find the image that best agrees with the interferometric data measured at a set of uv points (sparse uv coverage). To reconstruct images using the differential-phase method and the closure-phase method discussed in Sect. 2, we used, in both cases, the minimization algorithm ASA-CG (Hager & Zhang 2006), as described in Hofmann et al. (2014).

In *closure-phase methods*, the interferometric input data are the measured bispectrum elements of the target, which are calculated from the closure phases and visibilities measured at a set of uv points. In *Fourier-phase methods*, as the differential-phase method discussed in Sect. 2, the interferometric data are a set of measured Fourier spectrum elements calculated from the differential phases and visibilities.

To find the best target image, the χ^2 function between the measured interferometric data and the corresponding data of the actual iterated image has to be minimized in an iterative process. The χ^2 function of Fourier spectrum data is given by

$$\chi^2 := \int_{\mathbf{f} \in M^{(1)}} \left| \frac{O_k(\mathbf{f}) - O(\mathbf{f})}{\sigma(\mathbf{f})} \right|^2 d\mathbf{f}, \quad (\text{A.1})$$

where $M^{(1)}$ is the set of the two-dimensional spatial frequency coordinates \mathbf{f} of all measured Fourier spectrum elements $O(\mathbf{f})$ with their errors $\sigma(\mathbf{f})$, and $O_k(\mathbf{f})$ is the Fourier spectrum of the actual iterated image $o_k(\mathbf{x})$ (e.g., Eq. 11 in Hofmann & Weigelt 1993).

The χ^2 function of the four-dimensional bispectrum data of the closure-phase method discussed in Sect. 2 is given by

$$\chi^2 := \int_{\mathbf{f}_1, \mathbf{f}_2 \in M^{(2)}} \left| \frac{O_k^{(3)}(\mathbf{f}_1, \mathbf{f}_2) - O^{(3)}(\mathbf{f}_1, \mathbf{f}_2)}{\sigma(\mathbf{f}_1, \mathbf{f}_2)} \right|^2 d\mathbf{f}_1 d\mathbf{f}_2, \quad (\text{A.2})$$

as described in Hofmann et al. (2014). $M^{(2)}$ denotes the set consisting of the four-dimensional spatial frequency coordinates $(\mathbf{f}_1, \mathbf{f}_2)$ of all measured bispectrum elements $O^{(3)}(\mathbf{f}_1, \mathbf{f}_2)$ with their errors $\sigma(\mathbf{f}_1, \mathbf{f}_2)$, and $O_k^{(3)}(\mathbf{f}_1, \mathbf{f}_2)$ is the bispectrum of the actual iterated image $o_k(\mathbf{x})$ of the target.

Because of the sparse uv coverage and the noise in the data, a weighted regularization function has to be added to the above χ^2 function (in both methods) and the resulting function, the cost function, has to be minimized, as described in Hofmann et al. (2014).

The IRBis processing of the η Car data was performed as described in Hofmann et al. (2014). As start image of the reconstruction process, we used a Lorentz function. The width of the Lorentz function in each spectral channel was determined by a fit to the measured visibilities. The FOV of the reconstruction region is 50 mas and the pixel grid used is 64×64 pixels.

The main image reconstruction parameters of IRBis are the size of a binary circular mask in image space and the strength of the regularization parameter. In order to find a good reconstruction, these two parameters are varied. The regularization functions "maximum entropy", "pixel difference quadratic", and "edge preserving" were tested. For the final reconstructions presented in this paper, we used the regularization function "pixel difference quadratic", which enforces smoothness in the reconstruction. For each regularization function, 18 different sizes of the binary circular mask and 30 different regularization parameters were tested. From all these reconstructions in each spectral

channel, the reconstruction with the smallest value of the image quality parameter q_{rec} was chosen as image reconstruction result (q_{rec} is a quality measure including the χ^2 values, as described in Hofmann et al. 2014). The obtained images were convolved with the point spread function of a single-dish telescope with a diameter of 80 m.

Appendix B: Continuum-subtracted Br γ images

The image intensity distribution of the images presented in Figs. 4 to 6, and A.1 consist of the continuum and the line image components. In order to reveal the kinematics of signatures of the line-emitting gas more clearly, we additionally computed continuum-subtracted images. The continuum-subtracted images are presented in Figs. B.1 and B.2. They were computed in the following way. First, we computed the correct image brightness (i.e., not normalized) by multiplying the differential-phase images in Fig. 4 with the flux of the line at the corresponding velocity channel. From these images, we subtracted, in the next step, a continuum image (in differential-phase images, the relative position between the continuum images and the line images is known). As continuum image, we have computed the average of the continuum images at very high negative (in the range of -2574 to -2367 km s $^{-1}$) and high positive ($+1954$ to $+2162$ km s $^{-1}$) velocities (i.e., outside the line Br γ ; see green region of the spectrum in Fig. B.2). The continuum flux at each wavelength channel was derived from a linear fit of the continuum flux values outside the line.

As expected, dark gaps appear in images at negative velocities in the P Cygni absorption region. Obviously, the continuum at these negative velocities is smaller than the continuum outside the line because of P Cygni absorption. Therefore, the continuum-subtracted images do not show correct line intensity distributions in the inner continuum wind region (i.e., a region as large as the continuum wind) at radial velocities in the P Cygni absorption region.

However, outside these inner regions, the continuum-subtracted images allow us to see the Br γ line intensity distribution with high contrast. For example, the NW extension of the intensity distribution caused by the wind-wind collision zone discussed in Sect. 4.5 (paragraph on small radial velocities) is better visible in the continuum-subtracted images than in the other images. The low-velocity cavity component is best visible in the images at velocities in the range of $+35$ to $+109$ km s $^{-1}$.

In the images at velocities between about -78 and -28 km s $^{-1}$ in Fig. B.1, there are more small dots visible in the entire FOV than at other velocities. These dots are caused by the emission region that produces the well-known narrow emission line component at about -40 km s $^{-1}$. This narrow emission line component in the Br γ line of η Car is caused by the ejected, slow-moving objects B, C, and D (Weigelt & Ebersberger 1986; Hofmann & Weigelt 1988; Davidson et al. 1995, 1997) at separations from 0.1 to $0.3''$ (see Sect. 4). The ejected object B is partially located in the AMBER FOV and there may exist additional fainter structures of similar nature. This extended intensity distribution cannot be imaged with the VLTI because the VLTI baselines are too long to sample visibilities and phases of extended structures larger than about 50 mas. Therefore, this large extended intensity distribution breaks into many small dots in the reconstructed images.

Appendix C: Comparison of differential-phase and closure-phase images

In Fig. C.1, we compare contour line plots of the images reconstructed with the differential-phase and closure-phase methods to illustrate that both types of images show the fan-shaped structure.

Appendix D: Velocity dependence of size and photocenter shift

Figure D.1 presents the velocity dependence of the photocenter shift of the images in Fig. 4 (i.e., images of continuum plus line flux) with respect to the center of the continuum images. Figure D.2 shows the velocity dependence of both the image size and the photocenter shift of the images in Fig. 4 with respect to the center of the continuum images (velocities in the color bar are given in units of km s^{-1}).

Appendix E: Comparison of observed interferometric quantities with the same quantities of the reconstructed images

In Figs. E.1 and E.2, we compare the measured visibilities, differential phases, and closure phases shown in Figs. 2 and 3 with the visibilities, differential phases, and closure phases derived from the images reconstructed with the differential-phase method to check whether the interferometric quantities of the reconstructed images approximately agree with the observations.

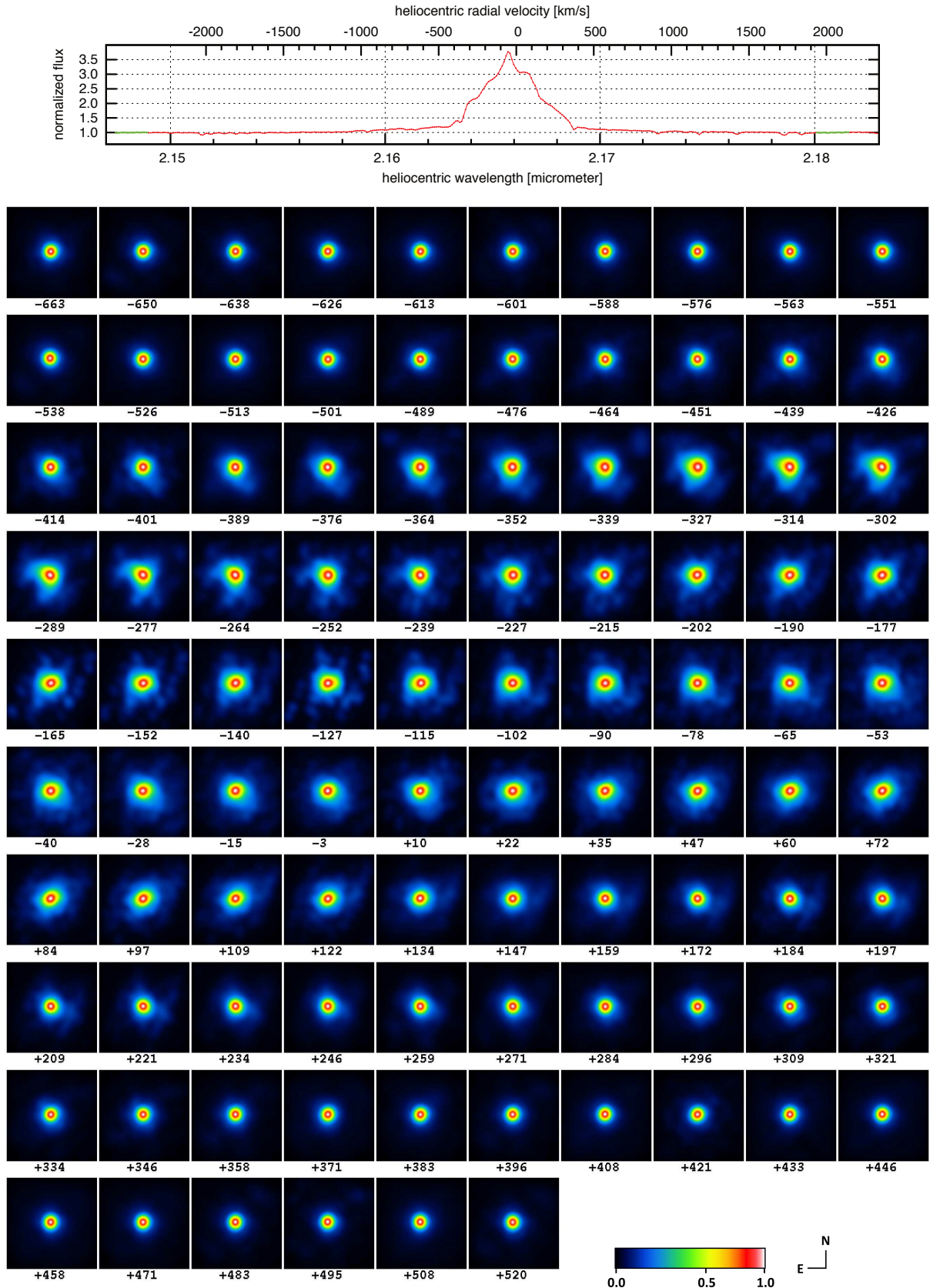


Fig. A.1. Same as Fig. 4, but the images were reconstructed with the closure-phase method (see Sect. 2; the FOV of the images is 50×50 mas or 118×118 au; 1 mas corresponds to 2.35 au).

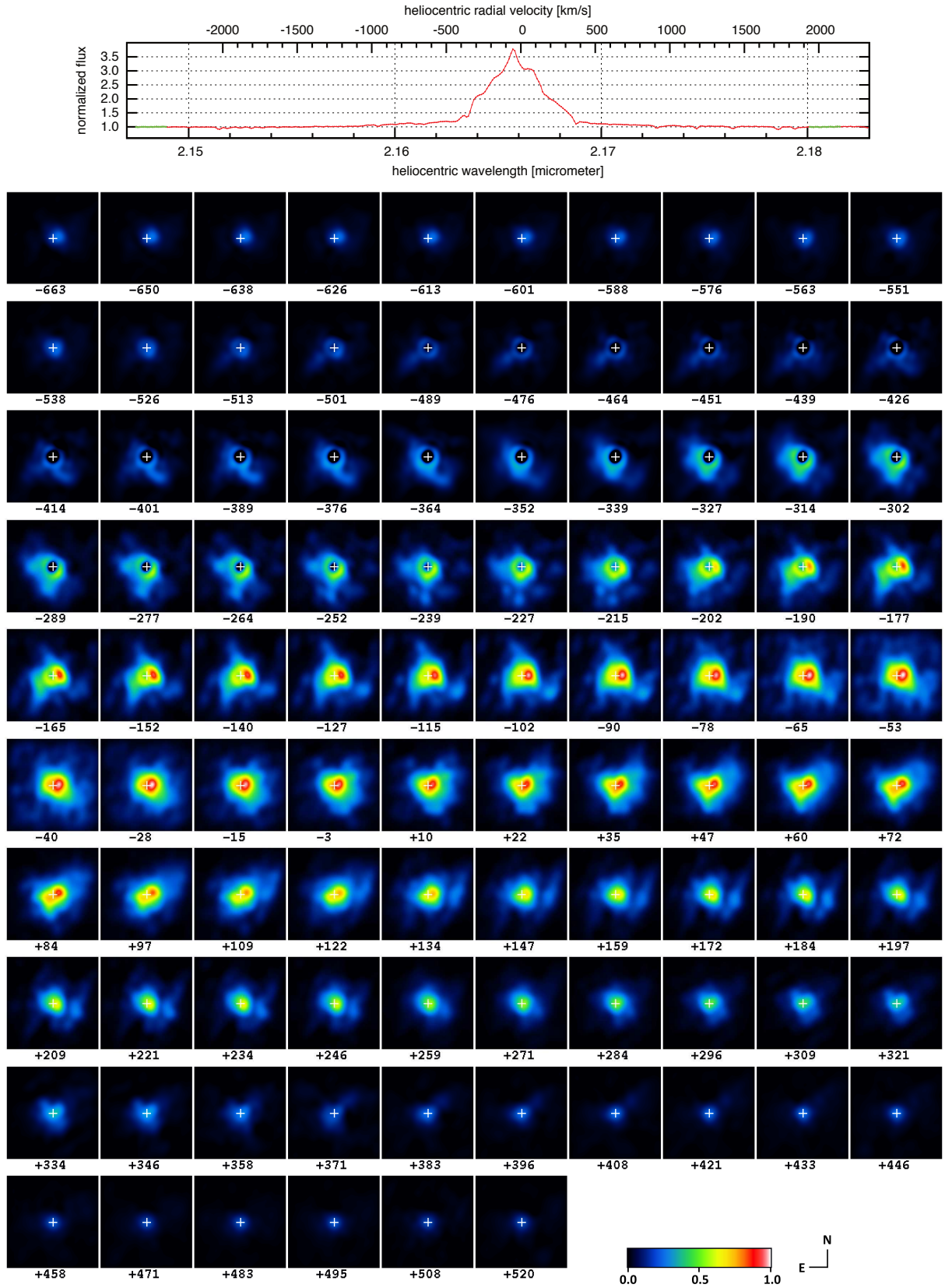


Fig. B.1. Continuum-subtracted Br γ images (see Sect. 4 and Appendix B; the FOV of the images is 50×50 mas or 118×118 au). The continuum-normalized spectrum at the top is the average of all spectra of the data listed in Table 1. The white crosses mark the central position of the continuum wind.

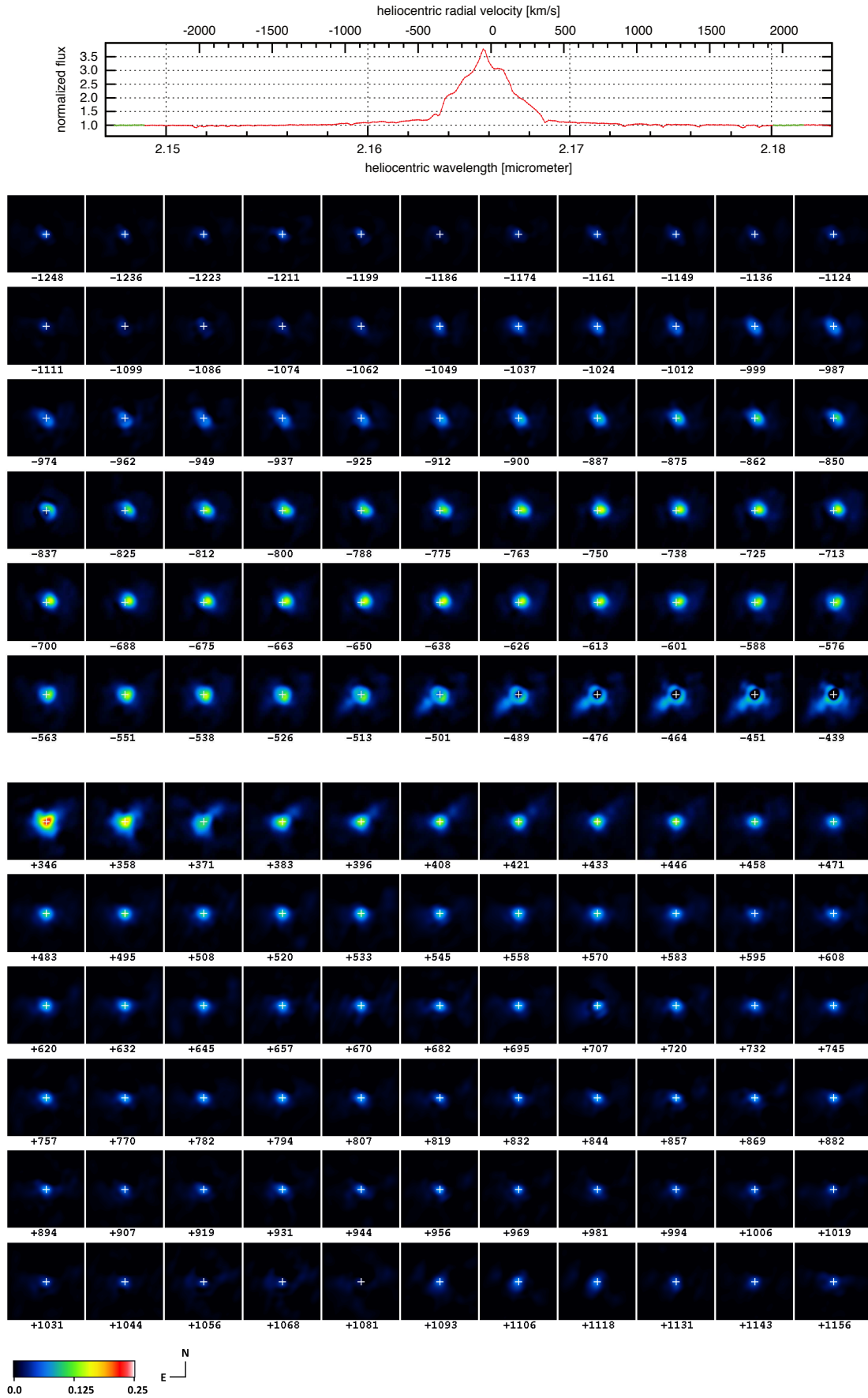


Fig. B.2. Continuum-subtracted Br γ images at high negative and positive velocities (see Sect. 4 and AppendixB). A different color code is used in this figure compared to Fig. B.1 to enhance the faintest structures. The white crosses mark the central position of the continuum wind.

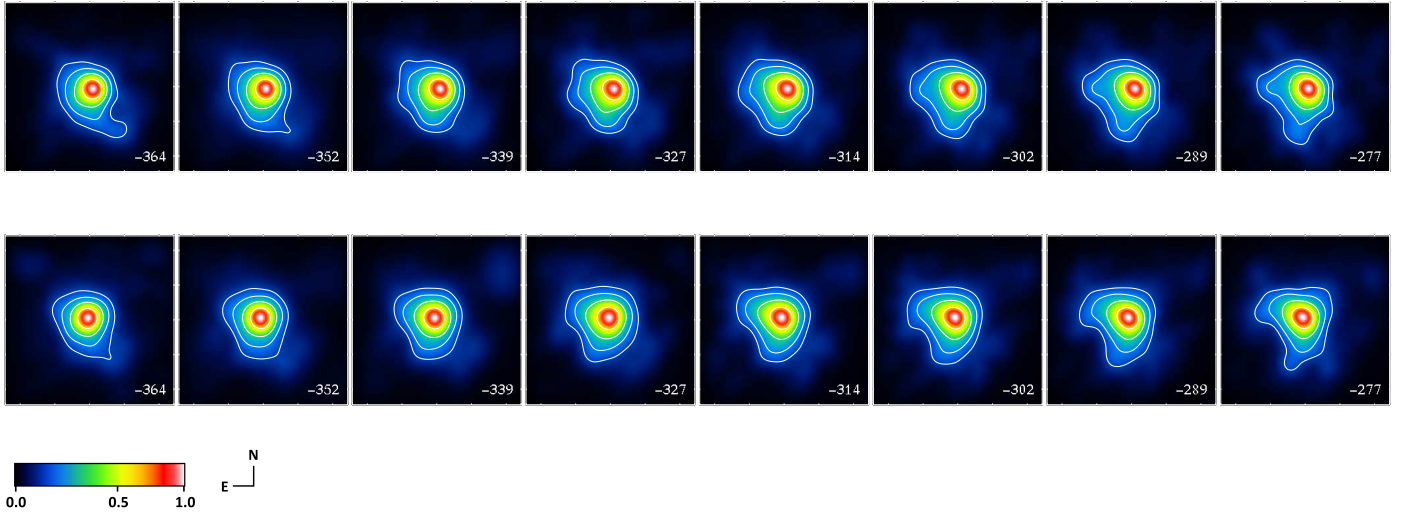


Fig. C.1. Comparison of the fan-shaped images reconstructed with the differential-phase (top) and closure-phase (bottom) image reconstruction method at velocities between -364 and -277 km s^{-1} (the FOV of the images is 50×50 mas or 118×118 au). Contour lines are plotted at 8, 16, 32, and 64% of the peak intensity.

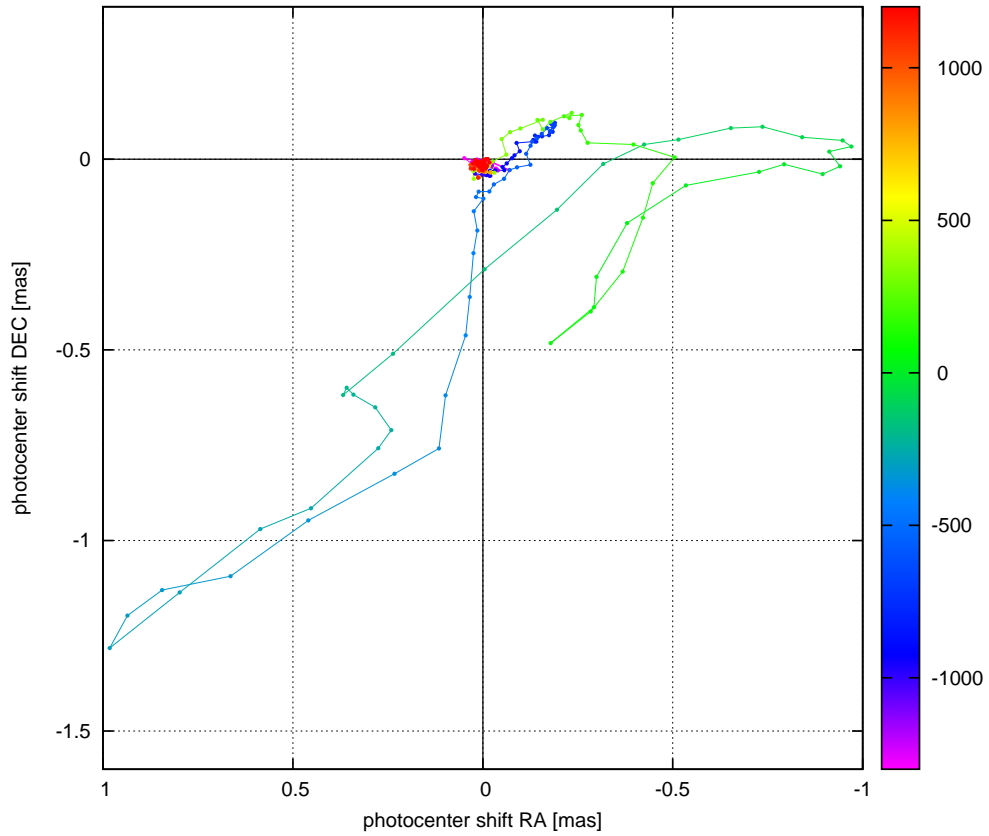


Fig. D.1. Velocity dependence of the photocenter shift of the images shown in Fig. 4 with respect to the center of the continuum images (velocities in the color bar are given in units of km s^{-1}).

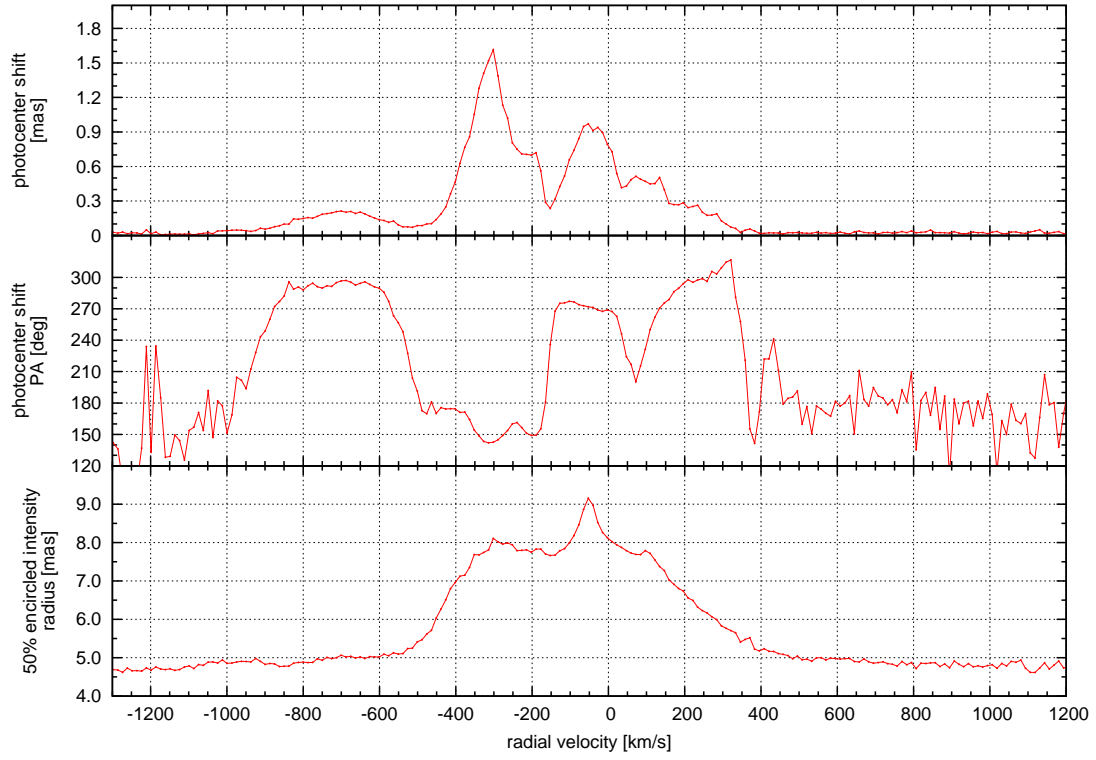


Fig. D.2. Velocity dependence of the size of the images in Fig. 4 (bottom) and the photocenter shift (both amount and PA of the shift) of the images shown in Fig. 4 with respect to the center of the continuum images.

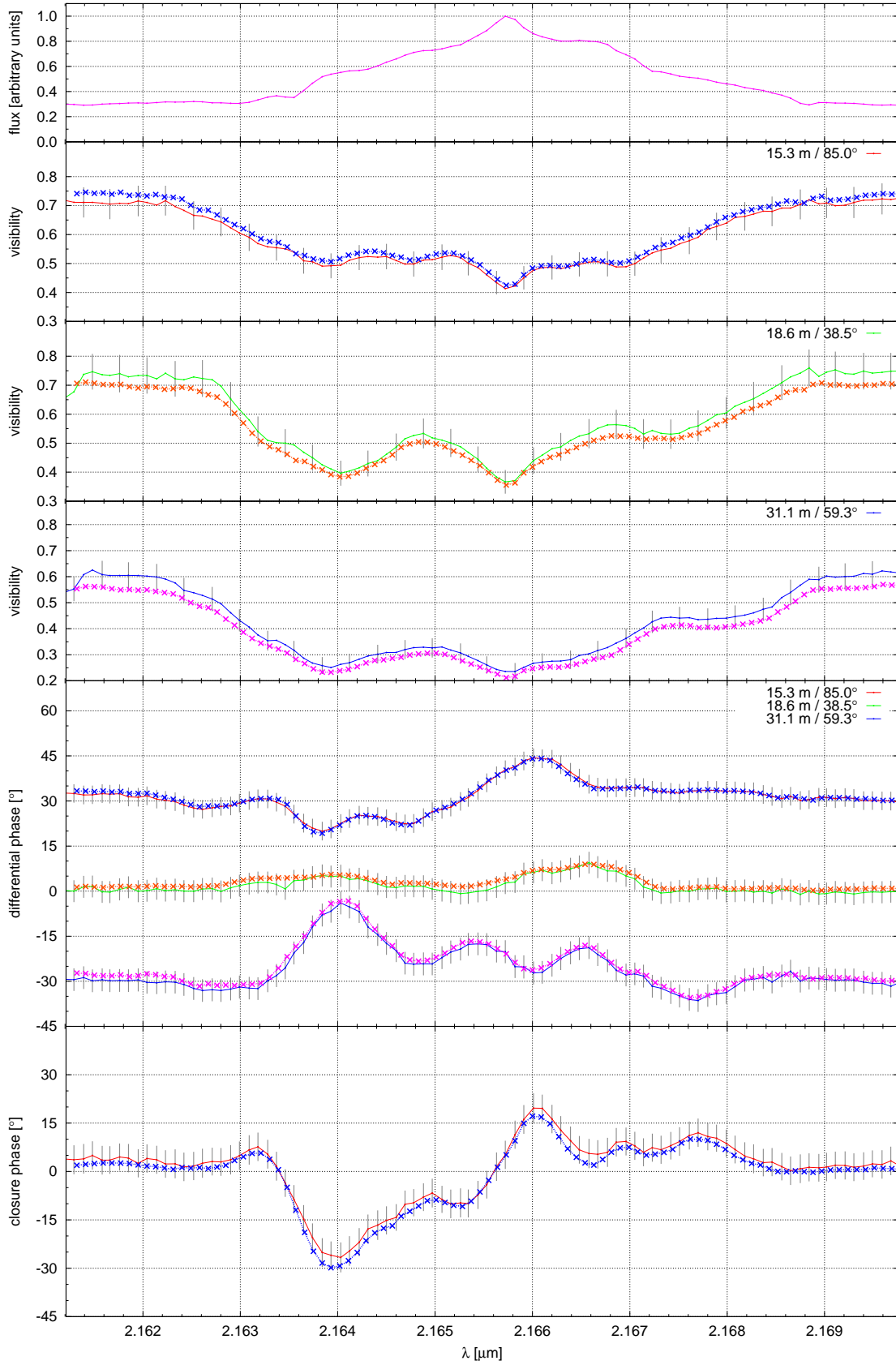


Fig. E.1. Comparison of the the measured visibilities, differential phases, and closure phases shown in Fig. 2 (curves with error bars) with the visibilities and phases derived from the images in Fig. 4 reconstructed with the differential-phase method (crosses).

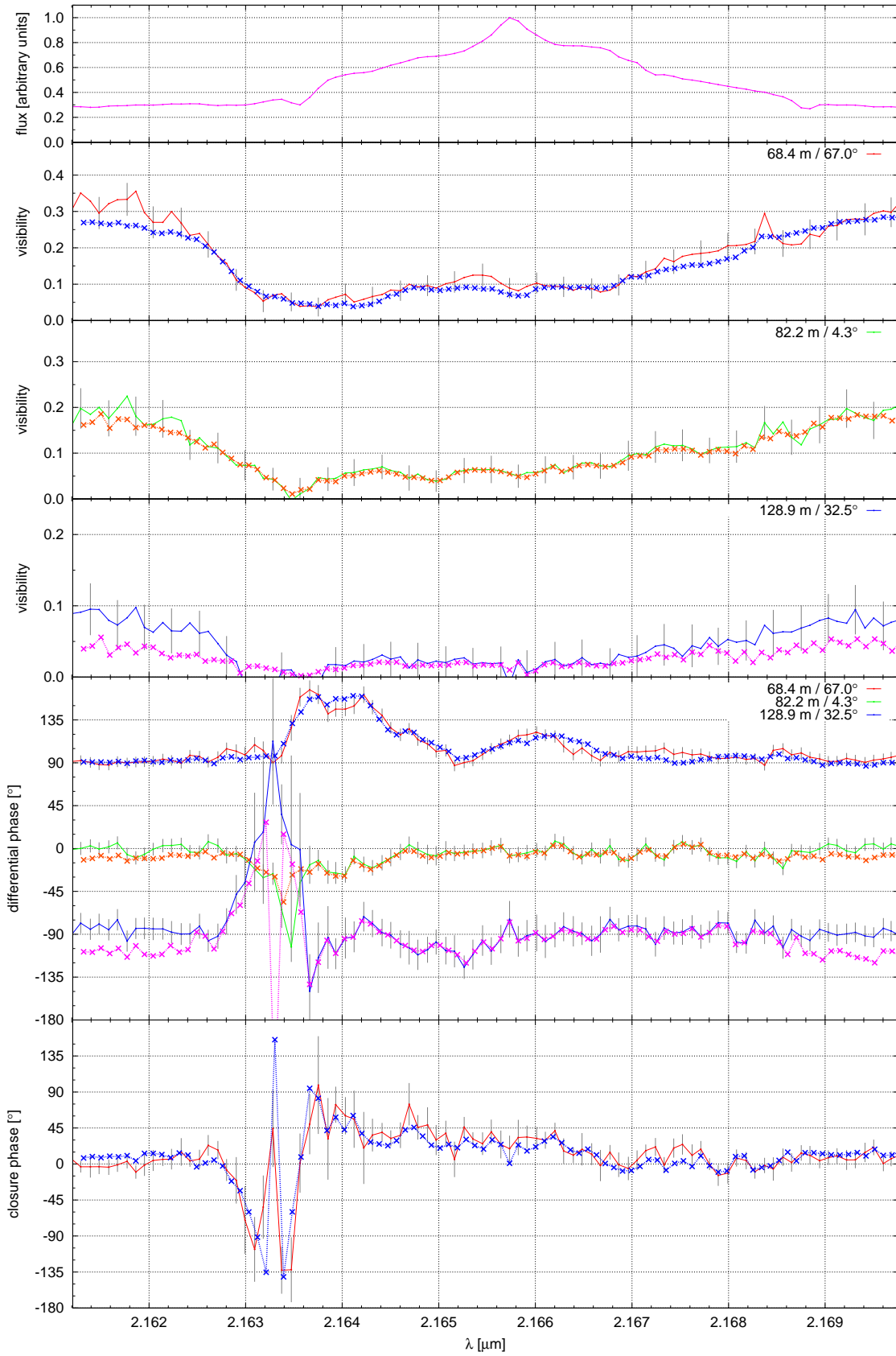


Fig. E.2. Same as Fig. E.1, but comparison for Fig. 3.